NASA Contractor Report 198052

Estimating Engine Airflow in Gas-Turbine Powered Aircraft with Clean and Distorted Inlet Flows

J.G. Williams and W.G. Steenken
GE Aircraft Engines
Cincinnati, Ohio

A.J. Yuhas
AS&M, Inc.
Edwards, California

Prepared for
NASA Dryden Flight Research Center
Edwards, California
Under NASA Lewis Flight Research Center
Contract NAS 3-26617

National Aeronautics and
Space Administration

Dryden Flight Research Center
Edwards, California 93523-0273

TABLE OF CONTENTS

LIST OF FIGURES

LIST OF FIGURES (Concluded)

LIST OF TABLES

NOMENCLATURE

A	Area, in^2
AIP	Aerodynamic Interface Plane
ALF	Aft looking forward
AOA	Angle of attack, deg
AOSS	Angle of Sideslip, deg
A_o/A_c	Capture area ratio**
C_{f1}, C_{f2}, C_{f3}	Flow coefficients for Methods 1, 2, and 3, respectively
DP/PC	Inlet total-pressure circumferential distortion descriptor**
DP/PR	Inlet total-pressure radial distortion descriptor**
ESN	Engine serial number
GEAE	GE Aircraft Engines, Cincinnati, Ohio
HARV	High Alpha Research Vehicle
IRP	Intermediate rated power (highest non-after-burning power setting)
LEX	Leading edge extension of the wing
M	Mach number
N1	Fan physical speed, rpm
P	Pressure, psi
PCM	Pulse code modulation
PLA	Power lever angle, deg
PSI	Pressure Systems, Inc., Hampton, Virginia
PS211 and PS212	Fan discharge static pressure measurements at engine station 2.1, psi
R	Specific gas contant for air, 53.36 ft-lbf/lbm ^oR
Re	Reynolds number
SPS	Samples per second
T	Temperature,
Tu	Turbulence**
U	Freestream velocity, ft/sec
W	Physical airflow, lbm/sec
W_c	Corrected airflow, lbm/sec
f	Function
g_c	Units conversion factor derived from Newton's second law, 32.174 lbm-ft/lbf-sec^2
n	Exponent in turbulent boundary layer velocity distribution
u	Velocity in boundary layer, ft/sec
y	Distance from boundary, in
δ	Boundary layer thickness, in
δ^*	Displacement boundary layer thickness
γ	Ratio of specific heats

** See Appendix A for definitions

NOMENCLATURE (Concluded)

Subscripts

Std	Standard day reference condition
a,b	Locations of wall static pressures
c	Duct centerline location
s	Static
t	Total
2	Engine inlet station
2.1	Fan station
5	Turbine station

ABSTRACT

The F404-GE-400 powered F/A-18A High Alpha Research Vehicle (HARV) was used to examine the impact of inlet-generated total-pressure distortion on estimating levels of engine airflow. Five airflow estimation methods were studied. The Reference Method was a fan corrected airflow to fan corrected speed calibration from an uninstalled engine test. In-flight airflow estimation methods utilized the average, or individual, inlet duct static- to total-pressure ratios, and the average fan-discharge static-pressure to average inlet total-pressure ratio. Correlations were established at low distortion conditions for each method relative to the Reference Method. A range of distorted inlet flow conditions were obtained from -10° to +60° angle of attack and -7° to +11° angle of sideslip. The individual inlet duct pressure ratio correlation resulted in a 2.3 percent airflow spread for all distorted flow levels with a bias error of –0.7 percent. The fan discharge pressure ratio correlation gave results with a 0.6 percent airflow spread with essentially no systematic error. Inlet-generated total-pressure distortion and turbulence had no significant impact on the F404-GE-400 engine airflow pumping. Therefore, a speed-flow relationship may provide the best airflow estimate for a specific engine under all flight conditions.

1.0 INTRODUCTION

Total engine airflow is a parameter used in a number of ways when addressing turbofan-engine-powered aircraft issues. For example, inlet distortion is often correlated with total-engine airflow (in the absence of inlet bleed, environmental control system bleed, or bypass flows) corrected to the aerodynamic interface plane (AIP), and AIP total engine airflow (physical or uncorrected) is an important part of the net thrust calculation. Our intent, as the title suggests, is to provide a means for estimating engine airflows under a variety of flight conditions with accuracies suitable to the needs at hand.

In static test cells, total-engine clean (undistorted) airflow can be obtained in a straightforward manner using calibrated bellmouths or venturis. While straightforward, the history associated with measuring total-engine airflow abounds with experiences marred by lack of attention to the issues required for accuracy and repeatability. In flight, these problems of accuracy and repeatability are made more difficult due to the presence of inlet flow distortion, instrumentation and data-acquisition-system space limitations, and changing thermal and pressure environments.

A unique opportunity was presented by the highly instrumented NASA High Alpha Research Vehicle (HARV) for addressing the difficult issue of providing reliable estimates of in-flight-determined total-engine airflow.

The HARV, an F/A-18A aircraft powered by two F404-GE-400 afterburning turbofan engines was specifically instrumented to accomplish propulsion-system-oriented research as part of its total mission and was flown at the NASA Dryden Flight Research Center. The propulsion mission was designed, in order of descending priority, to obtain distorted-flow AIP measurements during:

1) Stabilized high angle-of-attack/high angle-of-sideslip aerodynamic attitude conditions for comparison with computational fluid dynamic calculations,
2) Controlled maneuver transients to determine if differences exist between stabilized and transiently determined distortion measurements, and
3) Departed flight maneuvers.

Correlation of the flight-obtained measurements required knowledge of the AIP corrected inlet flow. This need was the inspiration for investigating a number of methods for estimating engine-corrected airflow in flight. Significant attention was given to the instrumentation and data acquisition/data reduction systems to assure they possessed state-of-the-art capabilities. Thus, the HARV aircraft allowed comparison of three different methods of correlating and estimating airflow with one method having three variants. Briefly, these are:

1) Engine corrected airflow correlated with fan corrected speed known as the flow-speed method (also referred to as the Reference Method).

2) Engine corrected airflow correlated with forms of the AIP static-pressure to total-pressure ratio. This method has three variants: A) the average wall-static pressure ratioed to the average total pressure, B) the rake-average static pressure ratioed to the individual total pressures, and C) the estimated local static pressures ratioed to the individual total pressures. These methods are given the shorthand notation of Methods 1, 2, and 3, respectively.

3) Engine corrected airflow correlated with fan-discharge static pressure ratioed to AIP total pressure (Method 4).

Crucial to the success of these efforts was the ground-test-cell flow calibration of the engine and the establishment of flow correlations for each method in flight at minimum inlet-flow-distortion conditions. These correlations then could be examined against the Reference Method (corrected flow - corrected speed) calibration at the fixed aerodynamic attitude conditions to determine if inlet distortion produced systematic deviations in the Methods 1, 2, 3, and 4 correlations, and which ones were least impacted by the effects of distortion.

The following sections of this report provide a description of the HARV aircraft, the instrumentation, each airflow estimation method, the method of calibration, the establishment of correlation functions, and the manner in which each correlation behaved in the presence of distortion and estimates of the systematic and random errors associated with each method. The report concludes with recommendations for the most optimum method for correlating and estimating engine airflow in the presence of high levels of inlet distortion.

2.0 TEST HARDWARE, DATA ACQUISITION, AND DATA REDUCTION SYSTEMS DESCRIPTIONS

The HARV aircraft, specifically configured to accomplish high angle-of-attack research, was highly instrumented and possessed state-of-the-art data acquisition and data reduction systems as described below. Further, the ground-test-cell calibration of the flight test engine and the results obtained are described.

2.1 HARV Aircraft Description

The HARV is a single-seat F/A-18A aircraft (preproduction aircraft Number 6) powered by two afterburning turbofan F404-GE-400 engines. The high angle-of-attack capability is obtained by thrust vectoring, in this case, by removing the divergent nozzle flaps from the convergent-divergent exhaust nozzle and deflecting the nozzle exit flow by inserting three externally mounted paddles into each exhaust stream in a controlled and coordinated manner to produce the desired thrust vectoring (Reference 1). This thrust-vectoring capability allowed achieving a wide range of stabilized angles of attack and sideslip at the desired Mach numbers of 0.3 and 0.4. The wide range of inlet conditions, in terms of inlet distortion to which the inlet was subjected, provided the database necessary for conducting the desired airflow correlation/estimation study.

The F/A-18 A aircraft inlets are two-dimensional, external compression inlets with 5-degree compression ramps mounted on the sides of the aircraft fuselage under the aft portion of the LEX (Leading Edge Extension of the wing) approximately 25 feet aft of the aircraft nose. Additional details of the inlet are described in Reference 2. The propulsion research was completed on the right-hand inlet aft looking forward (ALF).

The HARV aircraft and F/A-18 inlet system are shown in Figure 1.

2.2 F404-GE-400 Engine Description

The two F404-GE-400 engines that were installed on the HARV aircraft, during which the data discussed in this report were obtained, are Engine Serial Numbers (ESN) 310-083 installed on the left-hand side of the aircraft and 310-051 installed on the right-hand side of the aircraft. Both engines were equipped with an original engine control which placed the IRP flat at 87 degrees PLA.

ESN 310-051 had the standard complement of engine readout parameters as shown in Part A of Table 1. Additionally, flight test instrumentation was installed to provide additional readouts of bill-of-material parameters or additional parameters that were of interest to propulsion research. These parameters are listed in Part B of Table 1.

2.3 Ground Test Phase

The purpose of the ground test phase was to establish the test cell calibration of engine inlet corrected airflow with engine corrected speed for ESN 310-051 with bellmouth inlet (low distortion) conditions. Also, the use of fan-discharge-static-pressure/fan-inlet-total-pressure (cell ambient) ratio was investigated to determine if a better flow correlation could be established which took advantage of the fact that inlet distortion is attenuated as it passes through a compression component. With the total-pressure distortion attenuated, is was expected that the variation in static pressure would also be decreased. Thus, a few measurements averaged should give a reasonably valid estimate of the static pressure at the fan discharge.

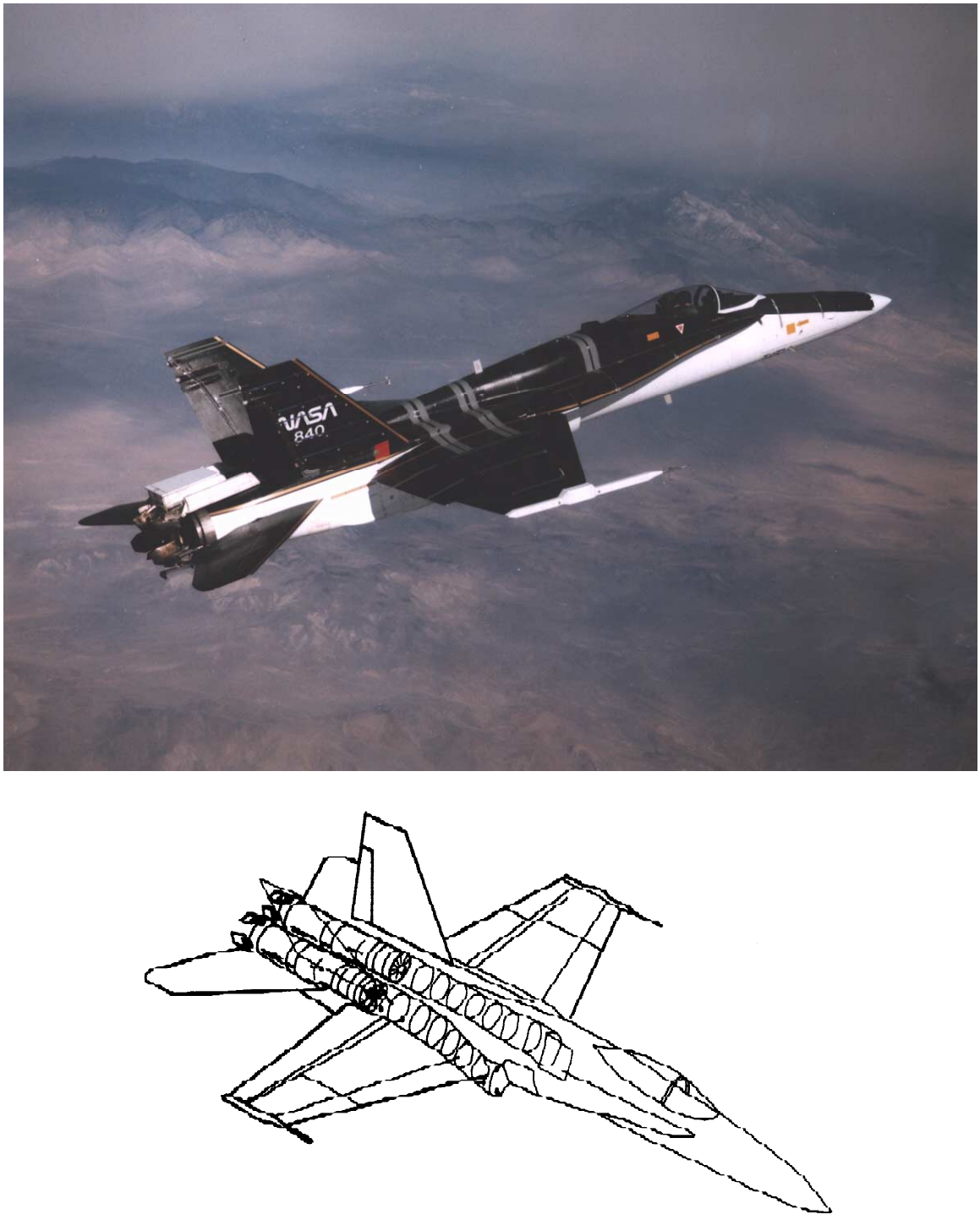

Figure 1. High Alpha Research Vehicle (HARV) and F/A-18 Inlet System.

Table 1. ESN 310-051 (Right-Hand-Side) ground and flight test instrumentation.

Part A - Bill of Material		Part B - Flight Test Instrumentation	
Instrumentation Designation	Instrumentation Description	Instrumentation Designation	Instrumentation Description
PLA*	Power Lever Angle	N1	Physical Fan Speed
TT1*	Engine Inlet Total Temperature	N2	Physical Compressor Speed
N1*	Physical Fan Speed	FVG	Fan Variable Geometry Position
N2*	Physical Compressor Speed	HPVG	Compressor Variable Geometry Position
FIGV	Fan Inlet Guide Vane Position	WFE	Engine Fuel Flow
CIGV	Compressor Inlet Guide Vane Position	WFET	Engine Fuel Temperature
CDP*	Compressor Discharge Pressure	WFABM	Afterburner Main Fuel Flow
WF*	Engine Fuel Flow	WFABMT	Afterburner Main Fuel Temperature
PT56*	Turbine Exhaust Pressure	WFABP	Afterburner Pilot Fuel Flow
EGT*	Exhaust Gas Temperature	PSFUELI	Control Inlet Fuel Pressure
A8*	Variable Exhaust Nozzle Position	PSFUELO	Control Outlet Fuel Pressure
		PS211, PS212	Fan Discharge Wall Static Pressures
		PSB1, PSB2	Combustor Wall Static Pressures
		PT56 (20)	Low Pressure Turbine Discharge Total Pressures
		PS6REF	Afterburner Inlet Reference Pressure
		PS6 (3)	Afterburner Inlet Wall Static Pressures
		PS7 (4)	Exhaust Nozzle Wall Static Pressures

* Parameters Also Used in Flight Test

This technique will only work if the effective exhaust nozzle area remains fixed with respect to engine corrected fan speed. This issue must be addressed for the F404-GE-400 engine since it employs T_5-corrected fan speed control limits. Thus, it is possible for the fan operating line to migrate under high T_2 conditions or for engines with very good performance.

The ground test-cell calibration data were obtained at the Edwards Air Force Base GEAE (Evendale, Ohio) Test Cell 2. Three down-power calibrations were conducted from maximum afterburner to idle. All the power calibrations were done in the same direction to mimimize the effects of control system hysteresis. In order to assure that the engine would run on the ground to corrected speeds as high as would be seen in flight, the fan speed schedule limit on the engine control was raised by 2.5 percent for ground testing only.

2.3.1 Test Cell Hardware

Test Cell 2 is an outdoor cell with a floor-mounted thrust stand giving the F404-GE-400 engine a centerline location of approximately 4.5 feet above the floor. A 25 foot high wall stands 30 feet forward of the engine to prevent foreign object damage.

The field bellmouth with an inlet screen installed and two inlet pitot-static pressure rakes were used to obtain the desired data. Use of the standard four inlet pitot-static pressure rakes was precluded due to structural beam interference with the two lower rakes.

2.3.2 Instrumentation

The instrumentation used for obtaining the data to establish the desired clean inlet flow correlations is listed in Table 1 Part A, the PS211 and PS212 parameters from Part B of the same table (GEAE test cell transducers were used rather than flight test transducers due to greater accuracy), as well as four inlet screen thermocouples, four bellmouth wall static pressures, and six total pressures and six static pressures from each of the two pitot-static rakes that were installed.

2.3.3 Results of Test Correlations

The relationship of engine corrected airflow with fan corrected speed is shown in Figure 2 for flows from idle to maximum afterburner. The root-sum-square uncertainty due to instrumentation accuracy, use of the field bellmouth, and limited bellmouth total-pressure instrumentation for undistorted inlet conditions is 1.6 percent.

The test cell relationship of engine corrected airflow with the fan-discharge-static-pressure/fan-inlet-total-pressure (cell ambient) ratio is shown in Figure 3 for reference purposes. The root-sum-square uncertainty is 1.9 percent if the T_5 limits do not become operative and 4.3 percent if the T_5 limits do become operative. If the limits do not come into play, then the root-sum-square uncertainty is more like the uncertainty given for the previous method. While the ground run data show evidence of operating line migration at high airflows, the flight test data obtained in the M=0.3 to M=0.4 range from 20 kft to 35 kft did not exhibit evidence of operating line migration.

The control scheduling of fan and core variable geometry, exhaust nozzle area, and turbine temperature showed that the engine operated within all F404-GE-400 production control limits. The engine measured inlet flow is within one percent of the F404-GE-400 status-cycle computer-model prediction.

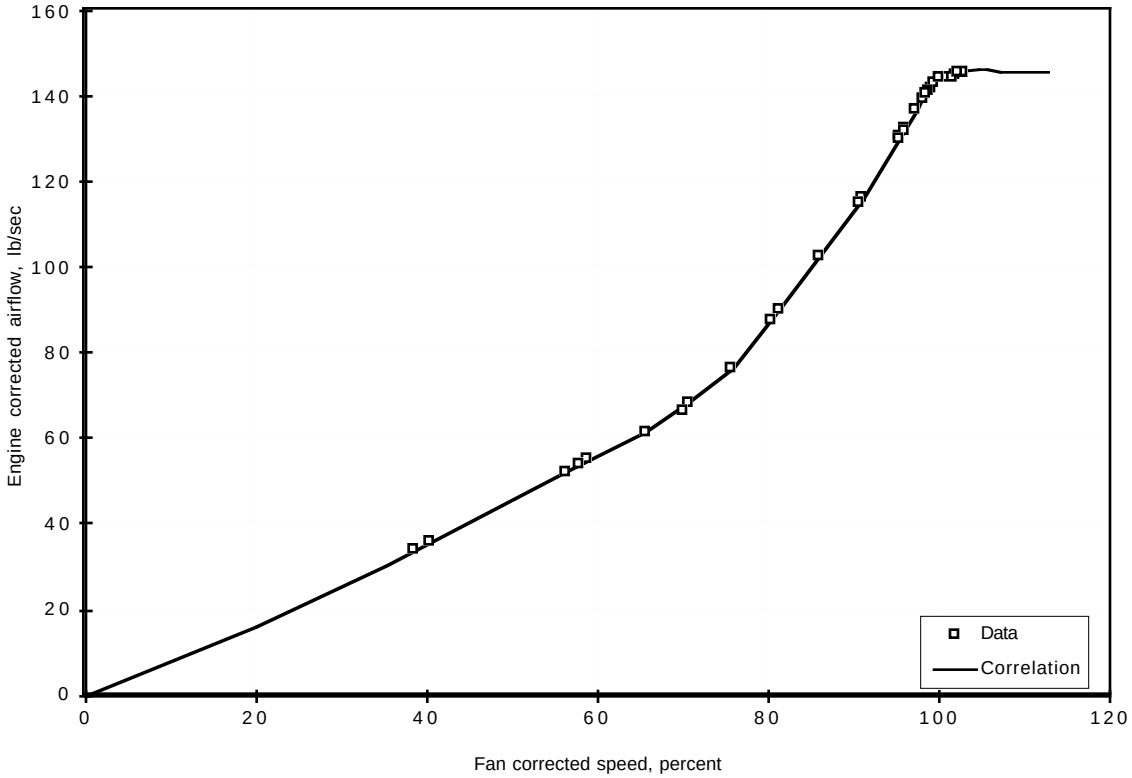

Figure 2. Ground test corrected flow to corrected speed data and correlation.

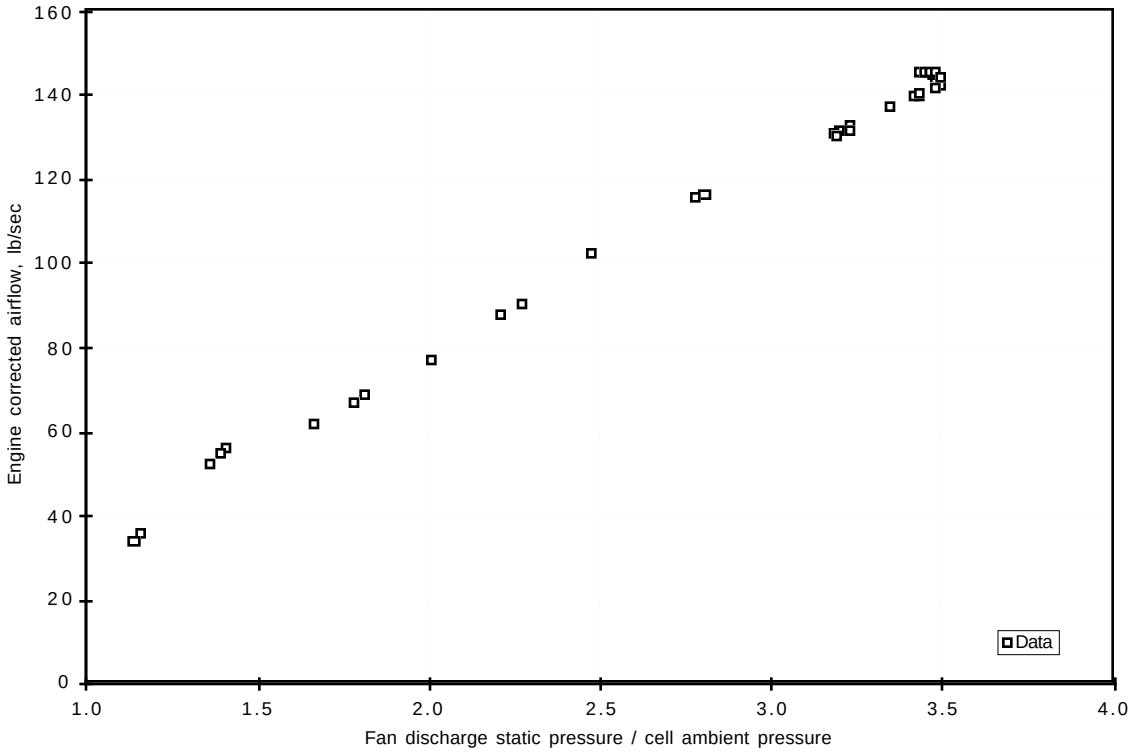

Figure 3. Ground test corrected flow to fan discharge static pressure / cell ambient pressure ratio correlation.

2.4 Flight Test Phase

During the flight test phase of this effort, in-flight flow correlation data were obtained during two flights that were specifically designed to provide low-distortion data. In-flight data with distortion levels varying from low to high were obtained during nineteen flights designed to obtain stabilized aerodynamic attitude data. Table 2 provides additional information regarding the flights from which the data used in this study were obtained.

In the following paragraphs, the special flight-test hardware that is germane to this flow correlation/flow estimation effort is described as well as the instrumentation, data acquisition, and data reduction systems.

2.4.1 Flight Test Hardware

The flight test hardware of special interest to the flow correlation and flow estimation efforts for this program is the AIP inlet-flow-distortion rake. The AIP is located approximately 4.0 inches forward of the engine bullet nose. This inlet distortion rake, which is fully described in Reference 3, provides both high-response and low-response (quasi-steady) measurements at forty total-pressure probes located on the centroids of equal areas for a five ring, eight rake array. It is the data obtained from the low-response probes that is of special interest in this study. It should be noted that the probe sensing configuration was designed to be very insensitive to flow angularity, an important criterion when measuring total pressure in distorted flows. Per Reference 3, this configuration allows the sensors to read true pressure levels at yaw angles over the range ±25 degrees and pitch angles from +15 to -25 degrees with positive angles being in the direction of the engine centerline. The flow blockage of the distortion rake structure at the AIP is 0.4 percent. The maximum blockage of the rake, which is less than eight percent, is located 1.5 inches downstream of the AIP.

In addition to the forty total-pressure probes located at the AIP, there were eight wall-static pressure taps located one between each total-pressure rake pair. Also, of importance to this effort were the fan discharge wall-static-pressure taps located downstream of the outlet guide vanes in the Plane 2.1 borescope holes.

The arrangement of the sensor locations at the AIP and at Plane 2.1 is shown in Figure 4.

2.4.2 Instrumentation and Accuracy

The AIP total and wall-static pressures described in Paragraph 2.4.1 were measured using PSI (Hampton, Va) differential-pressure transducers. The absolute pressures, using these transducers, are obtained using an accurately measured reference pressure and adding it to the differential pressures. The Plane 2.1 pressures were measured using absolute pressure transducers. The ranges and accuracies of the transducers are given in Table 3. The low-response instrumentation system for the PSI transducers was capable of performing an in-flight calibration. The calibration system allowed for the reference-pressure pneumatic source to be supplied simultaneously to each side of the PSI differential pressure sensors. These data allowed for any change in the zero intercept of the calibration to be removed and thereby increase the overall accuracy of the PSI transducers. The in-flight calibrations were performed at straight and level conditions prior to the execution of each set of flight research maneuvers.

Table 2. Test flights used in airflow correlation study.

Flight No.	Date	Purpose
211	3/16/94	Airflow Correlation Data – 1g Flight
241	5/11/94	
211–213	3/16/94	Stabilized Maneuver Data
214–216	3/18/94	
230–231	4/22/94	
232–233	4/28/94	
234–235	5/04/94	
236–237	5/05/94	
240	5/06/94	
241–243	5/11/94	
247	5/17/94	

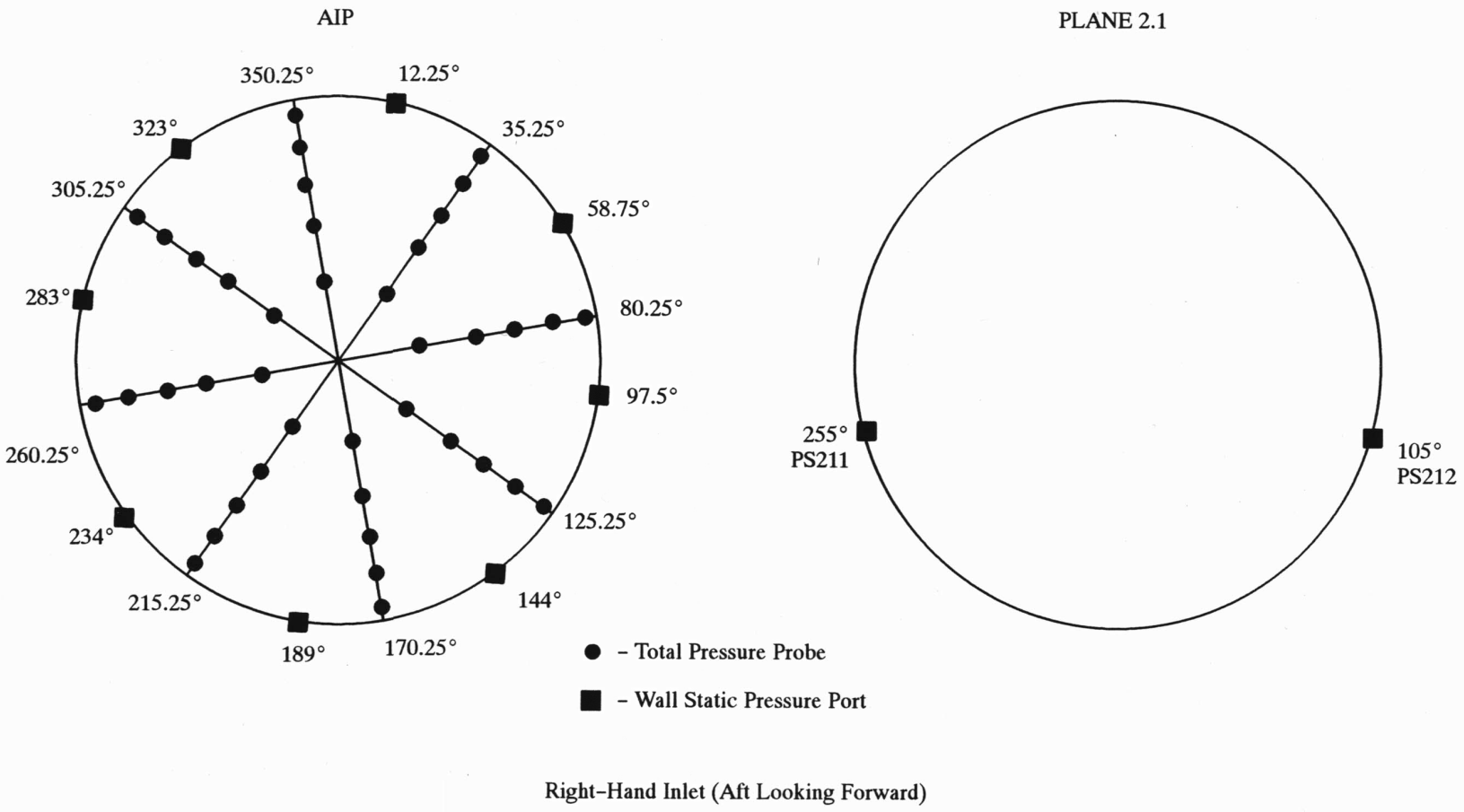

Figure 4. Pressure sensing locations.

Table 3. Pressure instrumentation ranges and accuracies.

Pressure Sensor Location	Manufacturer	Type	Range	System Accuracy
AIP Wall–Static and Total Pressures	PSI	Differential	±5.0 psid	±0.05 psi
AIP Reference Pressure	PSI	Absolute	0.4–19.0 psia	±0.025 psi
Plane 2.1	ENDEVCO	Absolute	0–50 psia	±0.50 psi

There were other parameters of interest. One was fan rotor speed and it had an accuracy of ±132.7 RPM. The second was inlet temperature. For these studies, the engine T_1 sensor output with a bias correction was used (see Appendix B for further details). With the bias correction, the T_1 random error is approximately ±0.04 percent at temperatures in the range of approximately 435 to 515 °F. Lastly, the freestream total-pressure measurement was taken from the left (ALF) wing-tip-mounted airdata swivel probe (Reference 4) and has an accuracy of ±0.007 psi throughout the angle-of-attack range that encompasses the data in this report.

2.4.3 Flight Test Data Acquisition System

The PSI measured low-response pressures and the reference pressure were sampled at a rate of 67 SPS. The Plane 2.1 wall-static pressures were sampled at 800 SPS while the fan speed and the inlet temperature were sampled at 40 SPS. All of the AIP and reference pressures were recorded on-board the aircraft on a digital tape using a PCM system. All of the engine measurements were telemetered to a ground station using a different PCM system. Also, both PCM systems recorded an embedded time code which was taken from an on-board time code generator.

Data typically were edited into a six-second sample for flow correlation and fixed aerodynamic attitude distortion test points. The correlation data sample was taken after the flight condition had been stabilized for approximately 30 seconds. The fixed aerodynamic attitude distortion test points tended to be less stable. In these cases, the objective was to have the pilot hold Mach number, angle of attack, and angle of sideslip as constant as possible for six to ten seconds.

2.4.4 Flight Test Data Reduction

Each PCM data stream in raw counts was stored on NASA Dryden Flight Research Center computers. The embedded time code in each data stream was used to time tag each data sample. This allowed for data from both PCM systems to be merged into a single data set using a common time source. The raw count data were converted into engineering units using appropriate calibration curves. Then, a merged computer file was created for each fixed aerodynamic attitude condition containing the parameters required for data analysis. This computer file was reduced further by applying the appropriate in-flight calibration to the PSI transducers. The final reduced computer file was available to all members of the NASA/GEAE Propulsion Research Team.

3.0 AIRFLOW ESTIMATION TECHNIQUES

Before discussing the manner in which the flow-speed ground-test calibration was used to establish the flow correlations, it is appropriate to discuss the algorithms used to obtain flow for each estimation technique.

Five independent airflow estimation techniques were used: a fan corrected-speed-based technique, three techniques using the AIP static- and total-pressure measurements, and a technique based on the fan discharge static-pressure to average fan inlet total-pressure ratio. Details are provided in the following paragraphs.

3.1 Corrected Speed Algorithm (Reference Method)

Prior to the flight test phase, a series of calibration runs on the test engine were performed as described in Paragraph 2.3 of this report. From these calibration runs, inlet corrected airflow as a function of fan corrected speed was generated as previously shown in Figure 2.

$$W_c = f\left(N1 \Big/ \sqrt{T_t / T_{Std}}\right) \tag{1}$$

This calibration was considered to be the reference engine airflow estimation method (Reference Method) and is fundamental to the establishment of the various airflow correlations.

3.2 AIP Wall-Static-Pressure to Total-Pressure Ratio Algorithms

At the AIP, an inlet rake system was installed and wall static pressure ports were located as described in Paragraph 2.4.1. These rake wall-static- and total-pressure measurements were used in the Methods 1, 2, and 3 airflow estimation techniques.

The wall-static-pressure to total-pressure ratio algorithms provide estimation of the average or the summation of airflow values obtained from the compressible flow function for the particular total- to static-pressure ratios being used and the AIP duct area or the AIP local area associated with each probe. That is,

$$W\sqrt{T_t}\,/\left(P_t A\right) = f\left(P_s / P_t\right) \tag{2}$$

$$W_c = \left(P_{Std} / \sqrt{T_{Std}}\right) \cdot A \cdot \left(W\sqrt{T_t}\,/\left(P_t A\right)\right) \tag{3}$$

Thus, the average or local corrected airflows can be derived from the average or local static-pressure to total-pressure ratios and the AIP duct area or the AIP local area associated with each probe (see Appendix A for details).

3.2.1 AIP Average Wall-Static-Pressure to Average Total-Pressure Ratio (Method 1)

The Method 1 airflow estimation technique was based on the flow function corresponding to the pressure ratio of the AIP average wall-static pressure to the AIP rake average total pressure.

3.2.2 Estimated Rake-Average Static Pressures and Individual Probe Total Pressures (Method 2)

The Method 2 airflow estimation technique was based on the summation of the flow functions corresponding to the pressure ratios of a local wall static pressure for each probe location equivalent to the average of the two adjacent wall static pressures ((P_{sa} + P_{sb})/2 - see Figure 5A) ratioed to the AIP rake local total-pressure values.

3.2.3 Estimated Individual Probe Static Pressures and Individual Probe Total Pressures (Method 3)

The Method 3 airflow estimation technique was based on the summation of the flow functions corresponding to the pressure ratios of individual local static pressures to the AIP rake local total pressure values (see Figure 5B). The static pressure at each rake location is determined from a radial interpolation between the two adjacent wall static pressures (P_{sa} and P_{sb}) at a given rake location to a duct centerline value (P_{sc} - this latter value being equivalent to the average of all the wall static values).

3.3 Fan Discharge Average Static Pressure and AIP Average Total Pressure (Method 4)

The Method 4 airflow estimation technique was based on a correlation of the ratio of the average fan discharge static pressure to AIP average total pressure with the Reference Method airflow value. In equation form, this relation can be written as

$$W_C = f(PS_{21}/PT_2) \quad (4)$$

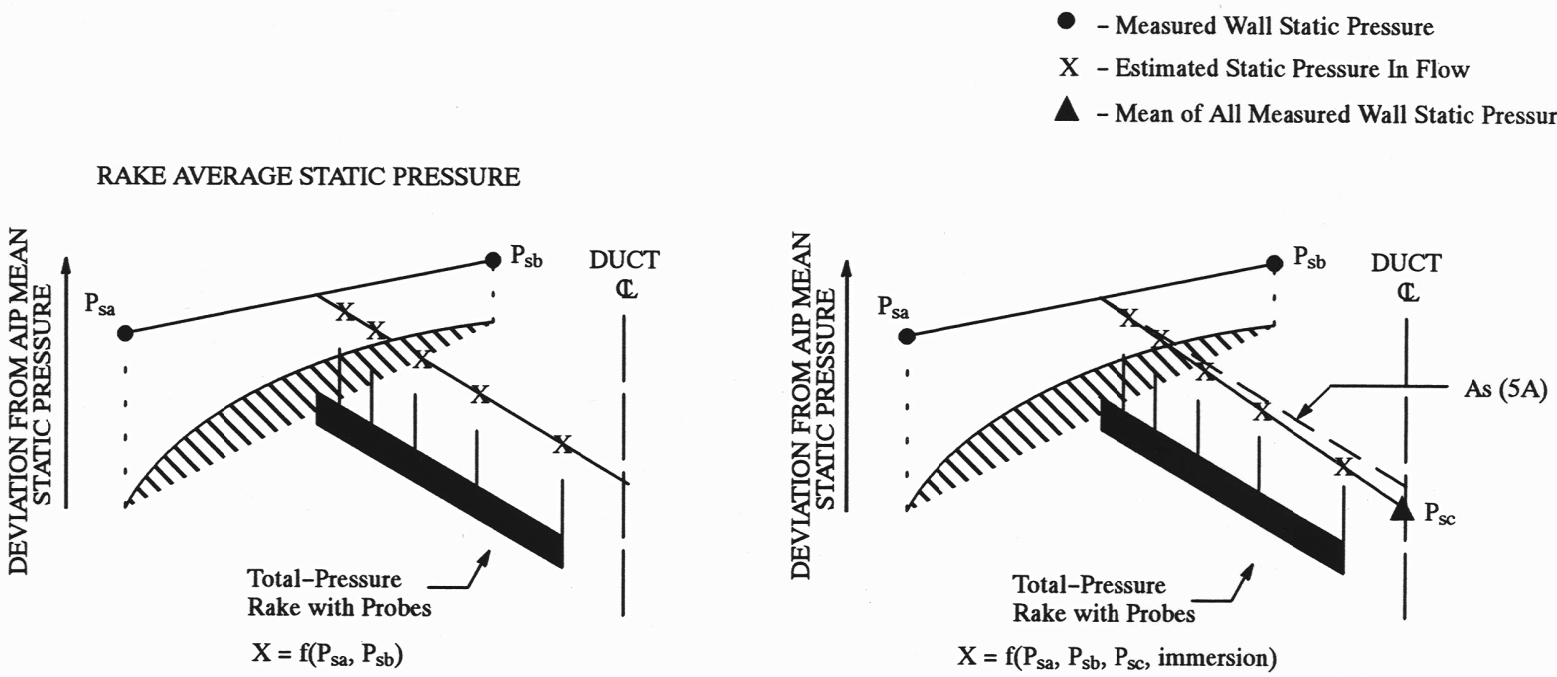

Figure 5. Interpolation techniques for estimating probe local static pressures.

4.0 DEVELOPMENT OF AIRFLOW CORRELATION TECHNIQUES

The Methods 1 through 3 for estimating airflow are based on relationships applicable to situations where the flow is uniform. In practice, the nonuniformities of the flow field lead to significant deviations of estimated flow based on the static-pressure and total-pressure measurements as compared to flow measurements obtained using flow straightening sections and calibrated venturis. In order to develop useful flow estimating techniques, Methods 1 through 3 as well as Method 4 must be correlated against a known standard, in this case, the ground speed-flow correlation and hereinafter referred to as the Reference Method. The purpose of this section of the report is to carefully and fully explain the correlations development methodology.

4.1 Methodology

The Reference Method airflow was based on the ground test-cell calibration as explained in Paragraph 3.1. This flow-to-speed relationship was assumed to be unchanged for stabilized in-flight operation at low distortion levels. This assumption is the fundamental building block upon which the development of the various correlations rests. Engine variable-geometry scheduling, which could affect this relationship, was confirmed to be unchanged from the ground test.

A series of in-flight calibration conditions were flown to correlate the various airflow methods to the reference flow-speed relationship. The prime in-flight calibration condition was high-power, 1g flight operation at Mach 0.6. At this condition, the inlet capture area ratio (A_O/A_C) (see Appendix A for details) was slightly less than unity, thus providing as ideal as possible flight-inlet-entry conditions with corresponding low inlet losses. The intention was to provide a condition where the inlet flow was as "clean" as possible for comparison with the ground calibration test. The in-flight calibration conditions were flown at two altitudes, approximately 20 kft and 35 kft, to assure that no significant altitude dependencies existed.

Subsequently, additional flight conditions at high power were examined which covered the range of Mach number conditions from approximately 0.4 to 0.9 and showed very similar characteristics as the Mach 0.6 data. Therefore, these were included also in the airflow calibration data set. In addition to the high power point airflows (maximum military), data were obtained at flows corresponding to part power, flight idle, and windmill power settings. The results obtained from these data are included also in the correlations. The Mach-altitude conditions at which the airflow calibration data were obtained are shown in Figure 6, the ranges of the capture area ratios are shown in Figure 7, and the ranges of angles of attack and sideslip are shown in Figure 8. The ranges of steady-state circumferential distortion and radial distortion, the ranges of static-pressure variations and steady-state distortions, and the turbulence and peak-to-peak planar wave levels at the AIP over which the correlations were established are shown in Figures 9, 10, and 11, respectively.

The various airflow estimation techniques were based on the data obtained during this testing. Excluding the fan corrected speed-based airflow, four procedures were developed. As previously stated, three of these were based solely on the pressure measurements at the AIP and the fourth was based on a fan-discharge static-pressure to fan-inlet total-pressure relationship. Details of these techniques are provided in the following paragraphs.

4.2 Definition of Flow Coefficients and Correlations

The flow coefficients (C_f) for Methods 1, 2, and 3 were defined using the ratio of the Reference Method airflow to the airflow calculated from the in-flight calibration data. Therefore, multiplication of a

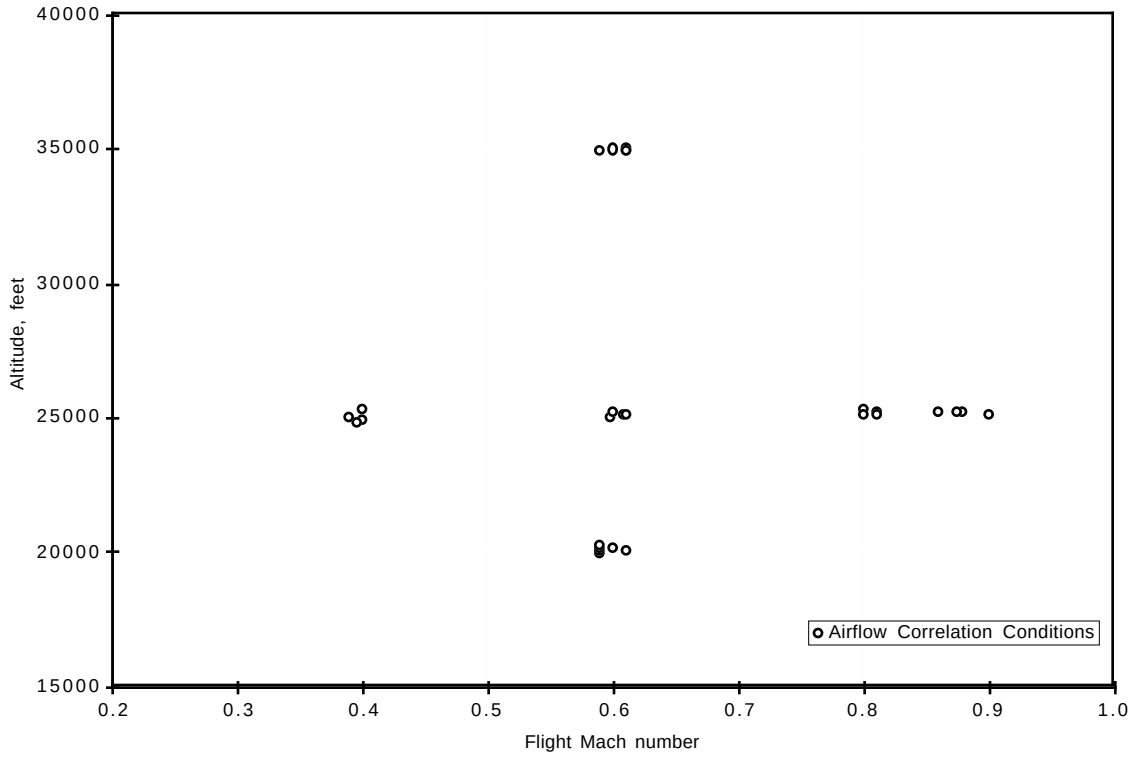

Figure 6. Mach number-altitude airflow correlation conditions.

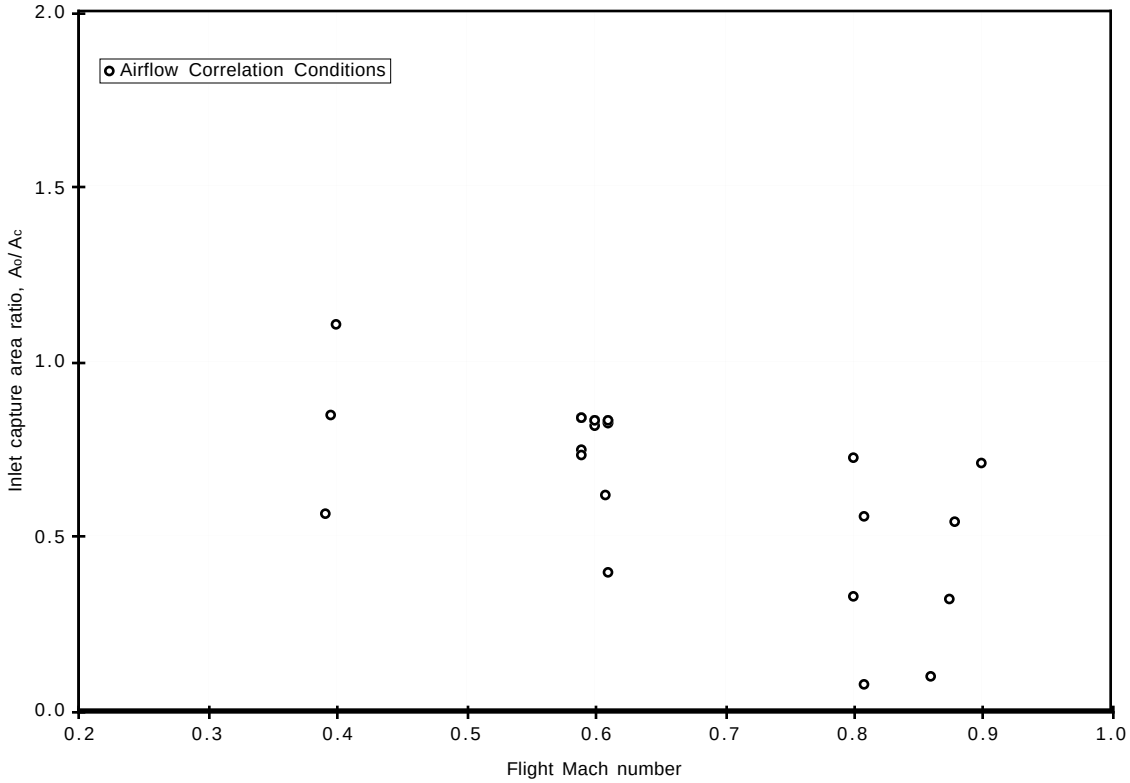

Figure 7. Inlet capture area ratios for airflow correlation conditions.

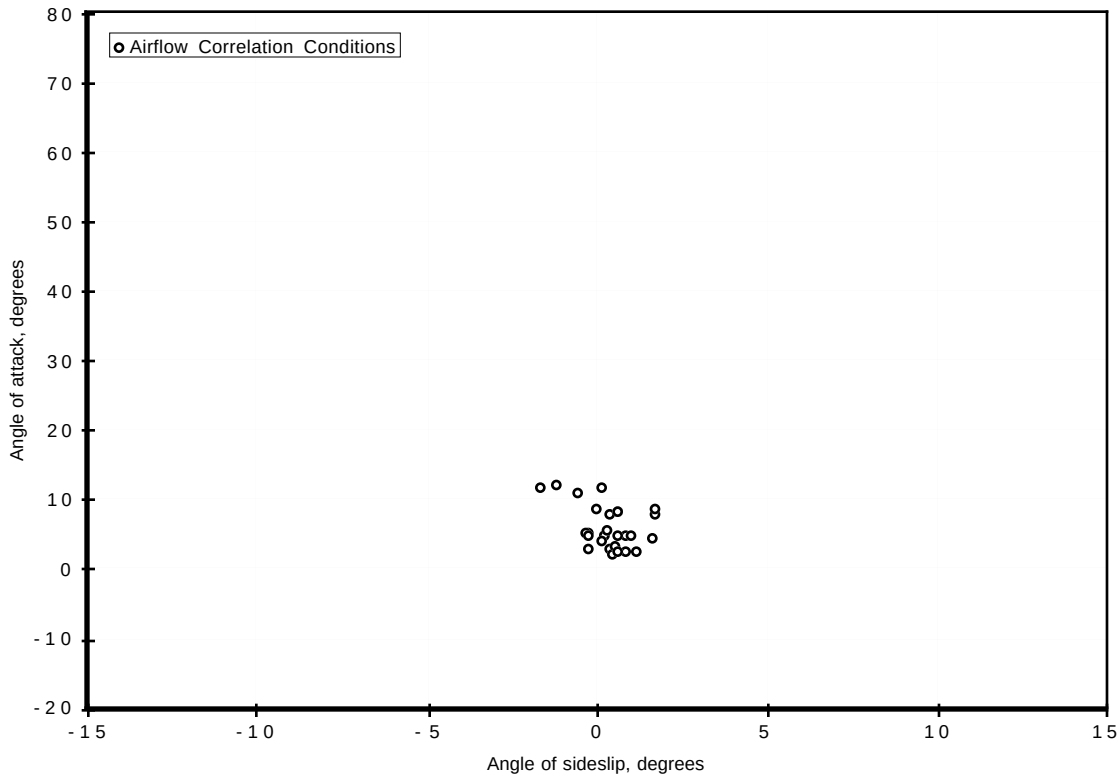

Figure 8. Angles of attack and sideslip for airflow correlation conditions.

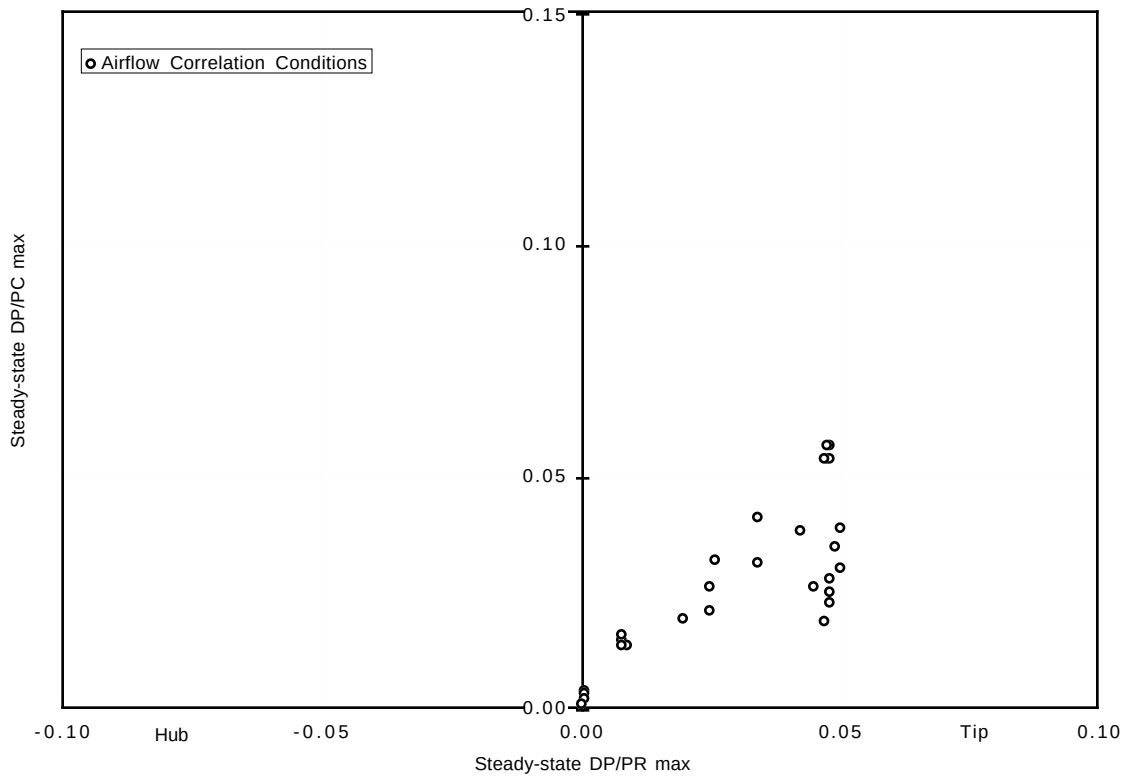

Figure 9. Steady-state circumferential and radial distortion levels for airflow correlation conditions.

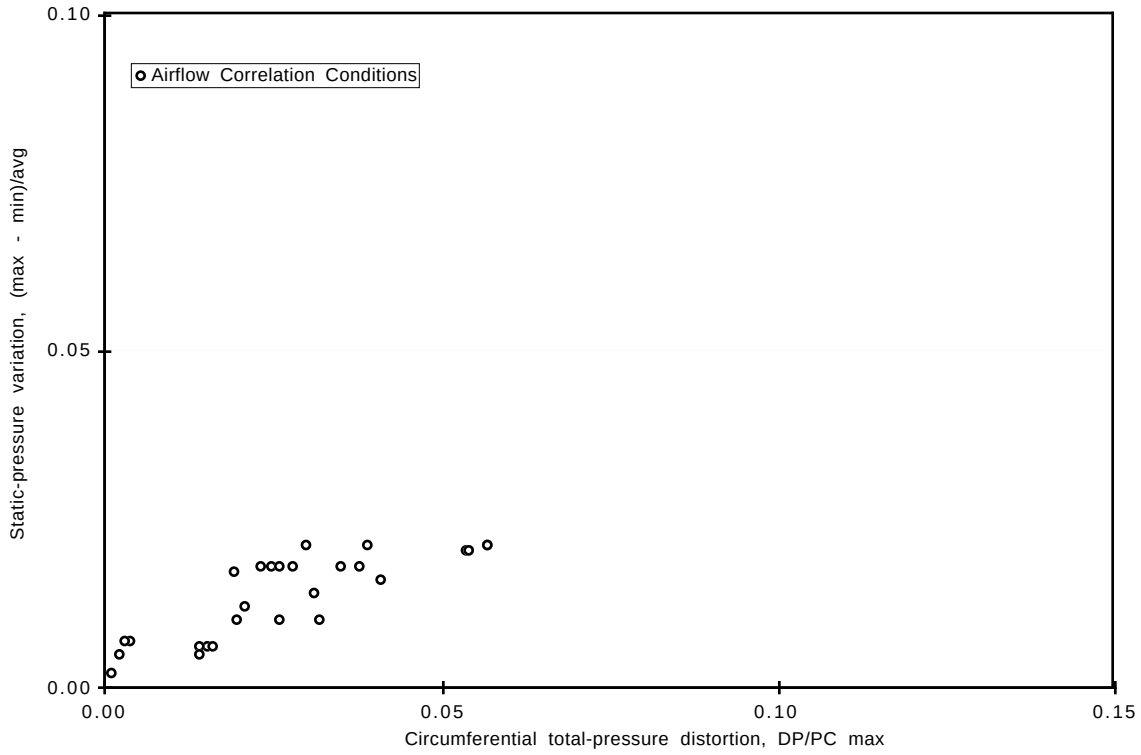

Figure 10. AIP static-pressure variations and steady-state circumferential distortion levels for airflow correlation conditions.

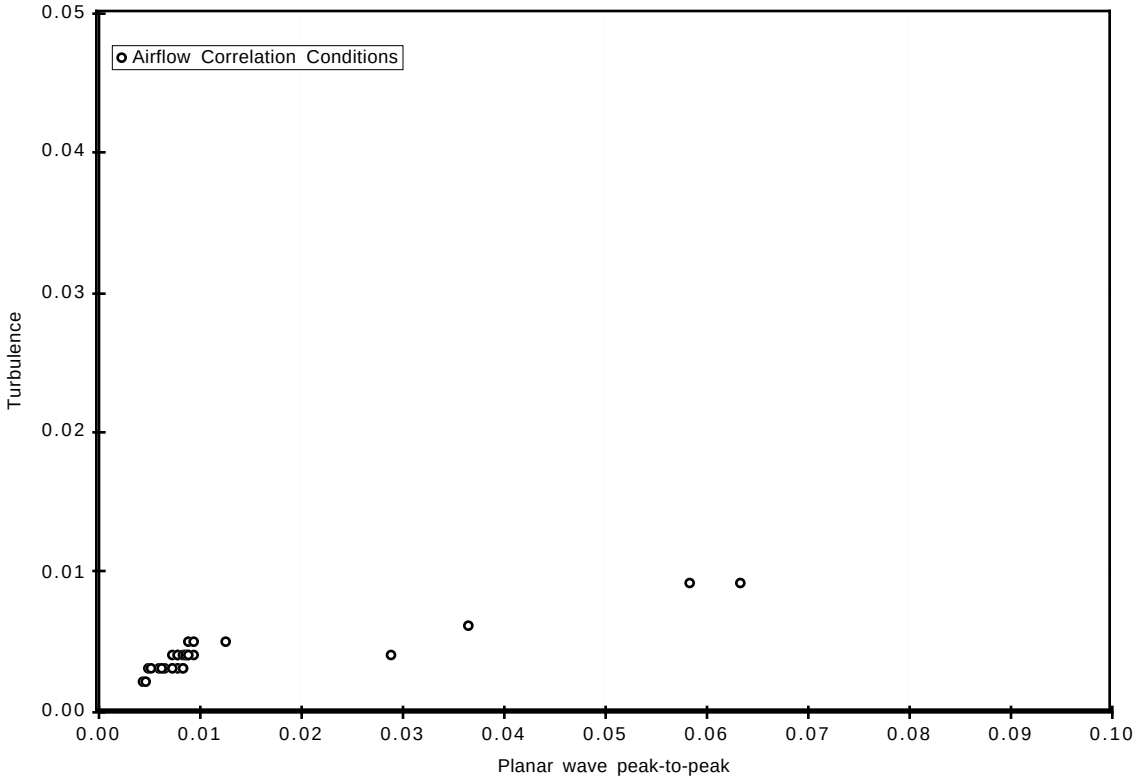

Figure 11. Turbulence and planar wave levels for airflow correlation conditions.

calculated airflow during flight by the appropriate C_f value approximates an airflow similar to the reference airflow level. Thus:

$$W_{c\ in\text{-}flight} = C_f \cdot W_{c\ calculated} \quad (5)$$

where $W_{c\ calculated}$ is derived from Equations 2 and 3, and

$$C_f = W_{c\ reference}/W_{c\ calculated} \quad (6)$$

From the calibration data set, the ratio of the reference to calculated airflow levels were used to define the general form of the flow coefficients for Methods 1, 2, and 3 as a function of calculated airflow. From each of these flow coefficient characteristics, a “best fit” relationship as a function of calculated airflow for the particular technique was defined. This was accomplished by fairing a curve through the data by hand on a piece-wise basis and minimizing the root-mean-square error.

An alternate procedure, designated Method 4, established the correlation of the ratio of average fan discharge static pressure to AIP average total pressure as a function of the corrected fan speed-based airflow. This relationship was established also from the in-flight calibration data according to Equation 4.

4.2.1 Method 1 Flow Coefficient - C_{f1}

Examination of the behavior of the Method 1 corrected airflow (Paragraph 3.2.1) as a function of the AIP average static pressure to average total pressure ratio (Figure 12) provides insight as to the magnitude of the difference between the calculated "ideal" flow based on the pressure ratio and physical area and the Reference Method airflow based on corrected speed. Figure 12 clearly illustrates the degree to which the ideal flow calculation overestimates the actual (Reference Method) corrected flow. This deviation is illustrated also by plotting corrected flow based on the calculated average pressures versus the corrected flow based on corrected speed as in Figure 13.

The form of the Method 1 flow coefficient characteristic as illustrated by the data points and the “best fit” relationship, which defines C_{f1} as a function of calculated airflow, are shown in Figure 14. The coefficients that provide the “best fit” relationship of C_{f1} as a function of the Method 1 calculated airflow are provided by Table 4.

4.2.2 Method 2 Flow Coefficient - C_{f2}

The Method 2 flow calculation results are shown plotted against the Reference Method airflow in Figure 15. The form of the Method 2 flow coefficient characteristic as illustrated by the data points and the “best fit” relationship, which defines C_{f2} as a function of Method 2 calculated airflow, are shown in Figure 16. The coefficients that provide the “best fit” relationship of C_{f2} as a function of the Method 2 calculated flow are provided in Table 4 also.

4.2.3 Method 3 Flow Coefficient - C_{f3}

The Method 3 flow calculation results are shown plotted against the Reference Method airflow in Figure 17. The form of the Method 3 flow coefficient characteristic as illustrated by the data points and the “best fit” relationship, which defines C_{f3} as a function of Method 3 calculated airflow, are shown in Figure 18. The coefficients that provide the “best fit” relationship of C_{f3} as a function of the Method 3 calculated airflow are provided in Table 4 also. The values are identical to those which define C_{f2}.

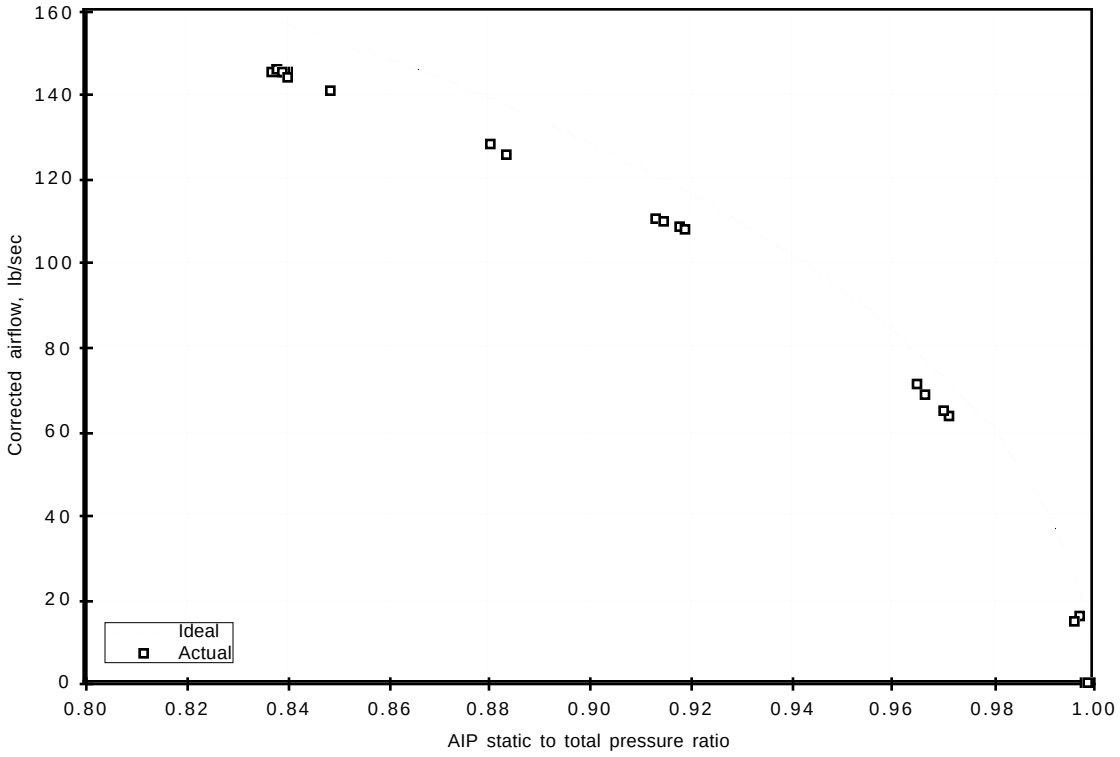

Figure 12. Airflow as a function of AIP static to total pressure ratio.

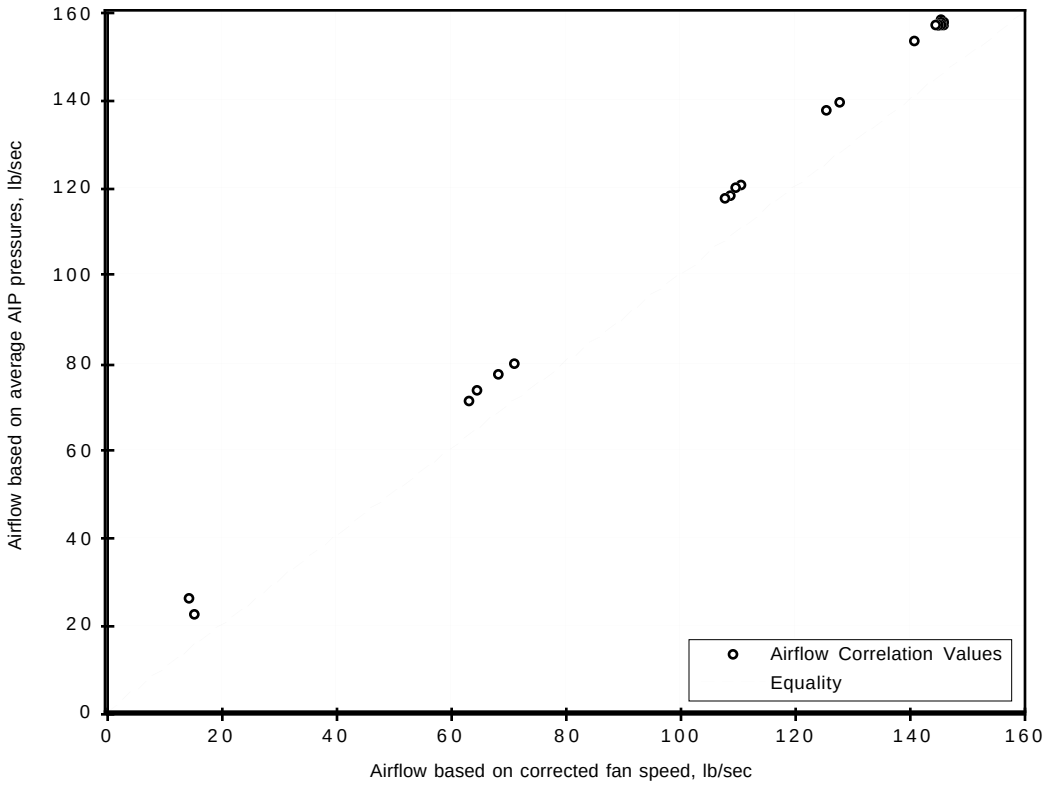

Figure 13. Corrected airflow based on AIP average pressures as a function of airflow based on corrected fan speed.

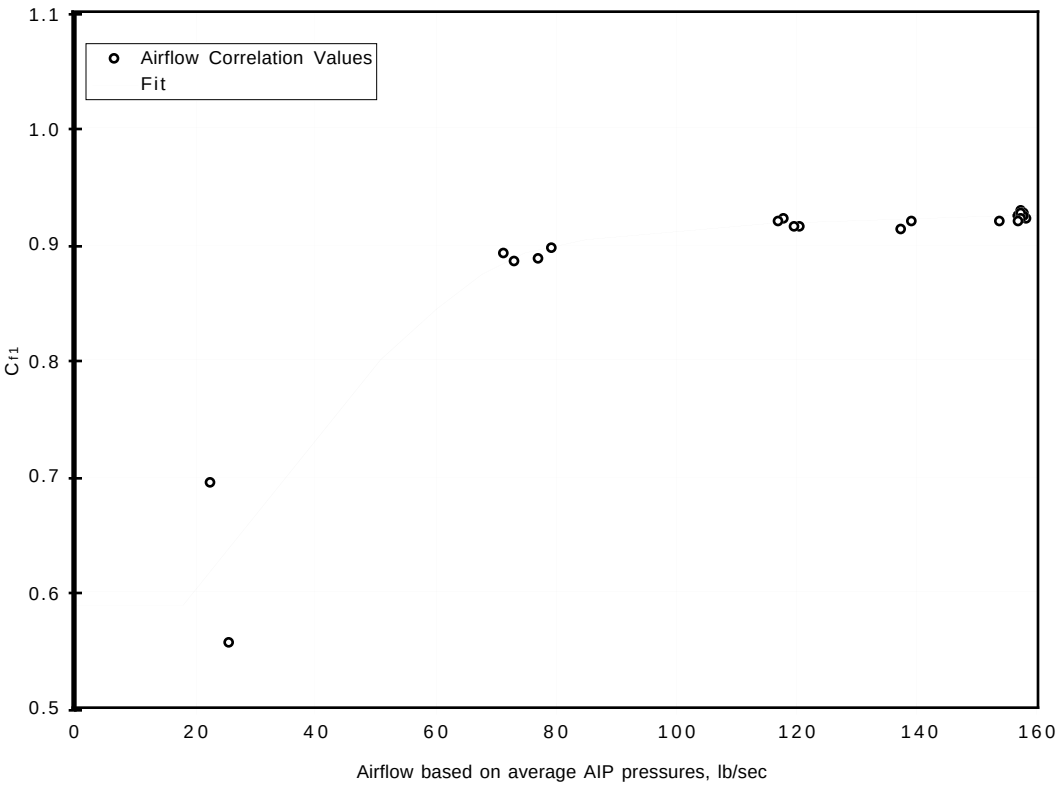

Figure 14. Method 1 flow coefficient relationship.

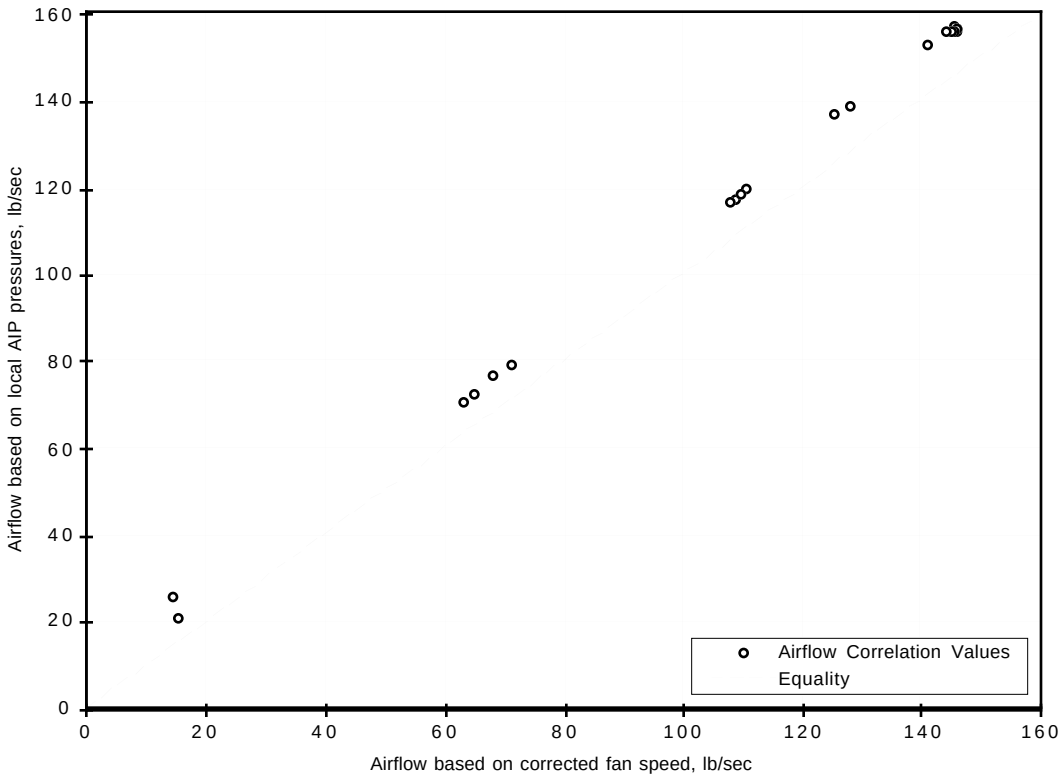

Figure 15. Corrected airflow based on AIP rake average static pressure and local total pressures as a function of airflow based on corrected fan speed.

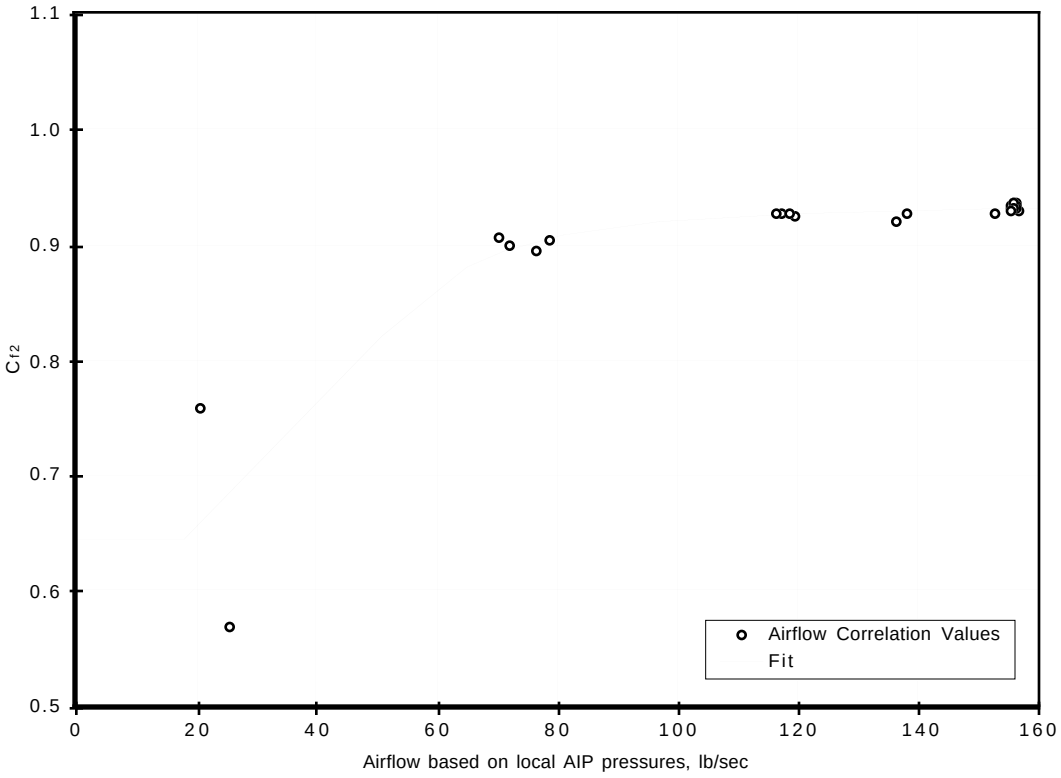

Figure 16. Method 2 flow coefficient relationship.

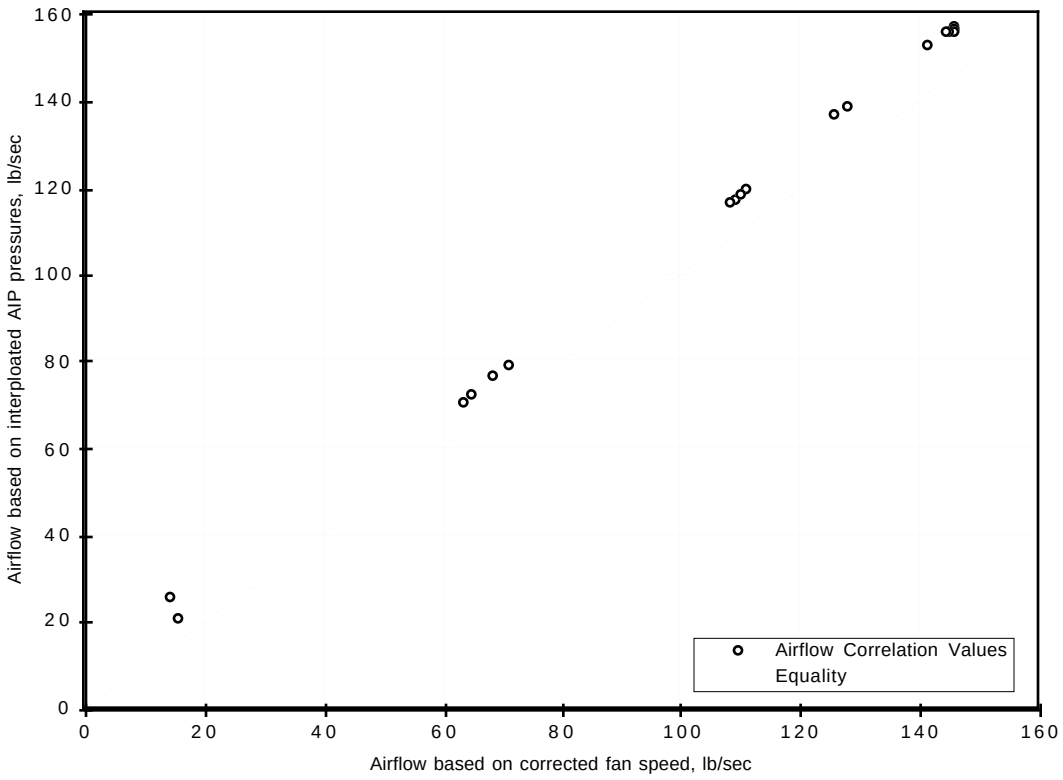

Figure 17. Corrrected airflow based on AIP estimated static pressures and local total pressures as a function of airflow based on fan corrected speed.

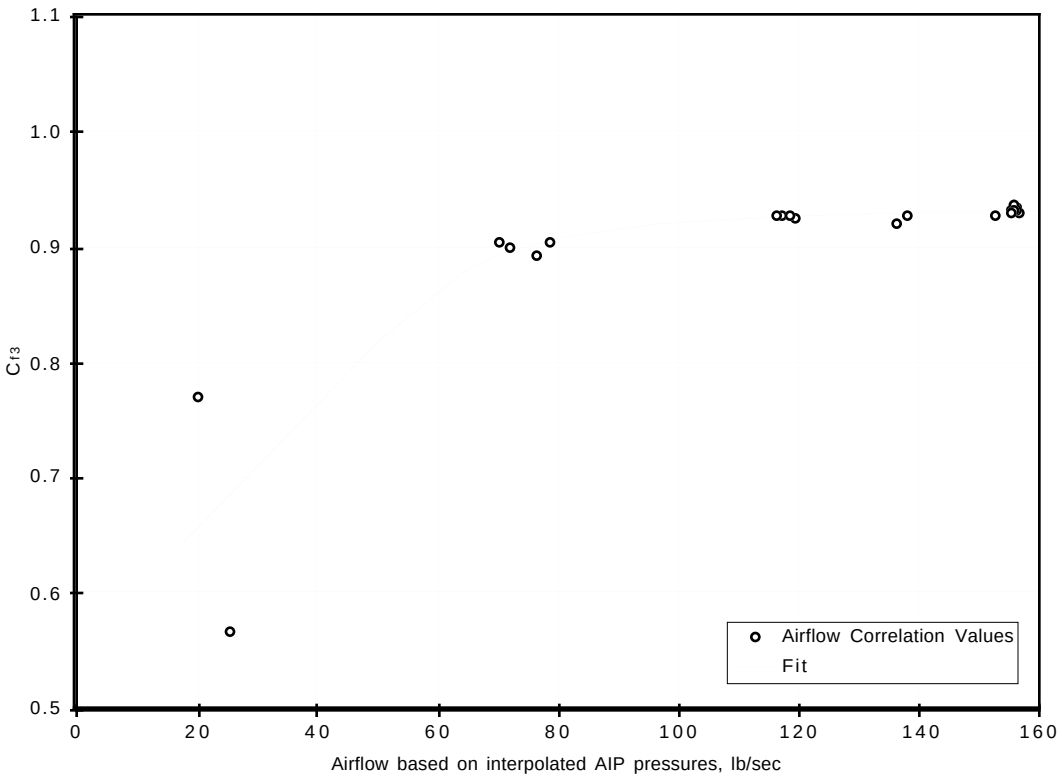

Figure 18. Method 3 flow coefficient relationship.

Table 4. Definition flow coefficients as a function of calculated airflow.

Calculated Airflow (lbm/sec)	Method 1 Flow Coefficient C_{f1}	Method 2 Flow Coefficient C_{f2}	Method 3 Flow Coefficient C_{f3}
<18.0	0.590	0.645	0.645
51.0	0.800	0.820	0.820
60.0	0.845	-	-
65.0	-	0.879	0.879
67.5	0.875	-	-
71.0	-	0.895	0.895
75.0	0.892	-	-
81.0	-	0.909	0.909
85.0	0.905	-	-
97.0	-	0.919	0.919
115.0	0.918	-	-
120.0	-	0.926	0.926
>155.0	0.926	0.931	0.931

4.2.4 Method 4 Flow Correlation

For the Method 4 airflow estimation technique, the correlation curve describing the "best fit" relationship of the ratio of average fan-discharge static pressure to AIP average total pressure as a function of the Reference Method airflow is shown in Figure 19. Table 5 defines the "best fit" relationship of the correlation as a function of the Reference Method airflow level.

Table 5. Definition of Method 4 flow correlation as a function of reference airflow.

P_{S21}/P_{T2}	Reference Airflow (lbm/sec)
0.96	0.0
0.96	15.0
1.10	34.0
1.30	47.1
1.60	61.2
2.00	80.0
2.67	109.3
3.00	121.8
3.20	130.0
3.40	138.4
3.50	142.5
3.55	144.1
3.60	145.0
3.65	145.4
3.72	145.7
3.80	145.9
4.00	146.0

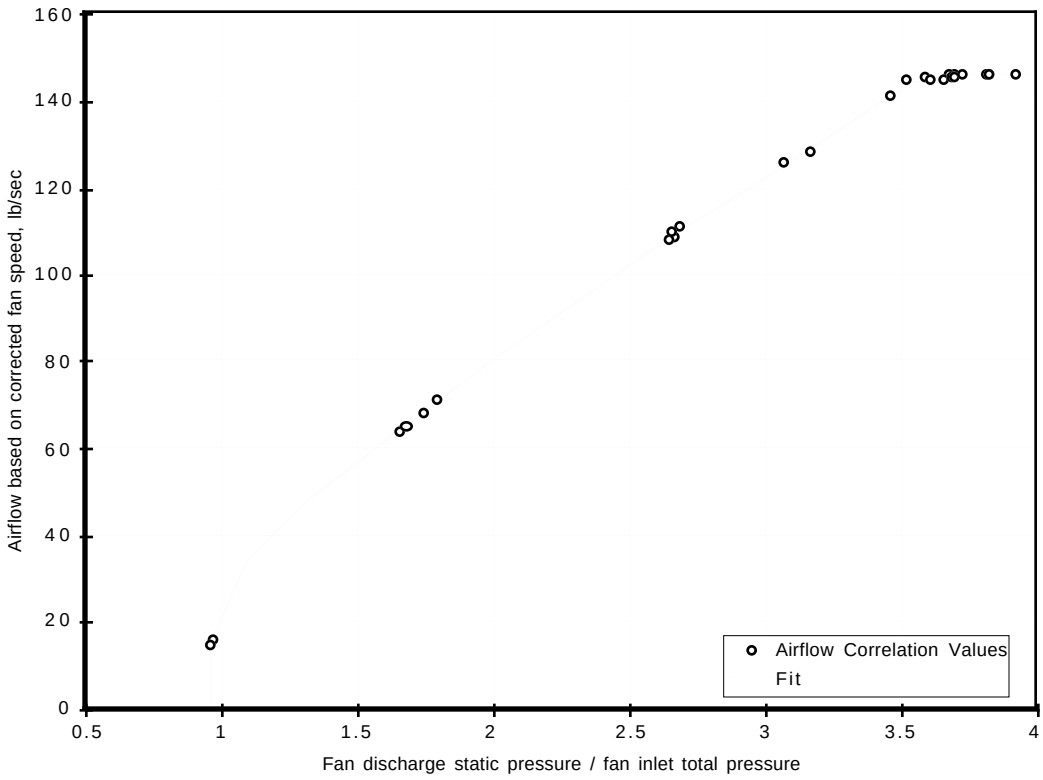

Figure 19. Method 4 flow correlation.

4.3 Flow Correlation Accuracies

Figures 20 through 23 illustrate the degree of correlation achieved by the Methods 1 - 4 techniques when plotted against the Reference Method airflow.

The relative accuracy in terms of the systematic (also known as fixed or bias) error and the random (also known as precision) error of the percentage difference between the reference and correlation estimate of the airflow levels for the in-flight calibration data sets are provided in Table 6 noting that the data set includes 24 data points.

Table 6. Systematic and Random Errors of Correlation Methods.

Method	Systematic Error	Random Error
1	0.067%	±0.428%
2	-0.007	±0.476
3	-0.001	±0.476
4	-0.041	±0.526

4.4 Contributions to Flow Coefficients

For Methods 1, 2, and 3, the difference in the flow coefficient values (Table 4) from unity is a consequence of the influences not accounted for in the one-dimensional airflow estimation techniques. At high power, the difference is 7 to 7.5 percent. This difference increases as the power setting decreases, being about 10 percent at flight idle and about 35 percent at a windmill condition.

The contributing influences affecting the derived flow coefficients include the AIP probe/rake blockage; the features of the airflow between the outermost probe and the duct wall, as well as any features in the AIP flow field not measured by the 40 element total-pressure probe array; the assumptions as to the spatial variation of static pressure across the AIP; the error in the assumed AIP physical area; the thermal effects on the duct hardware that change the AIP physical flow area; and the distortion levels present during the in-flight calibration conditions. A number of these details are discussed as follows.

The probe blockage, although not a large contributor, is about 0.4 percent of the physical AIP area.

One of the more significant contributing influences is the duct-wall boundary layer. A consequence of having the AIP rake total-pressure probes in area-weighted locations is that the annulus between the outermost AIP probe elements and the inlet duct wall represents 10 percent of the AIP physical area. The physical distance of the outermost probe from the duct wall is 0.712 inches. An estimation of the airflow in this region needs to take into account the presence of the duct wall boundary layer. The 40-element array at the AIP is the industry-standard for inlet distortion measurements, whereas for inlet airflow measurement, the instrumentation typically includes additional detailed measurements close to the wall to quantify the impact of the inlet boundary layer. The thickness of the inlet duct boundary layer was not directly measured. An estimate of the effect of boundary layer thickness on the derived airflow, and flow coefficient, can be made from the relationship of boundary layer growth as a function of duct Reynolds Number and assumptions about the shape of the boundary layer profile (Reference 5). The growth of boundary layer per unit duct length is approximated by the relationship $0.376\ (Re)^{-1/5}$. At an

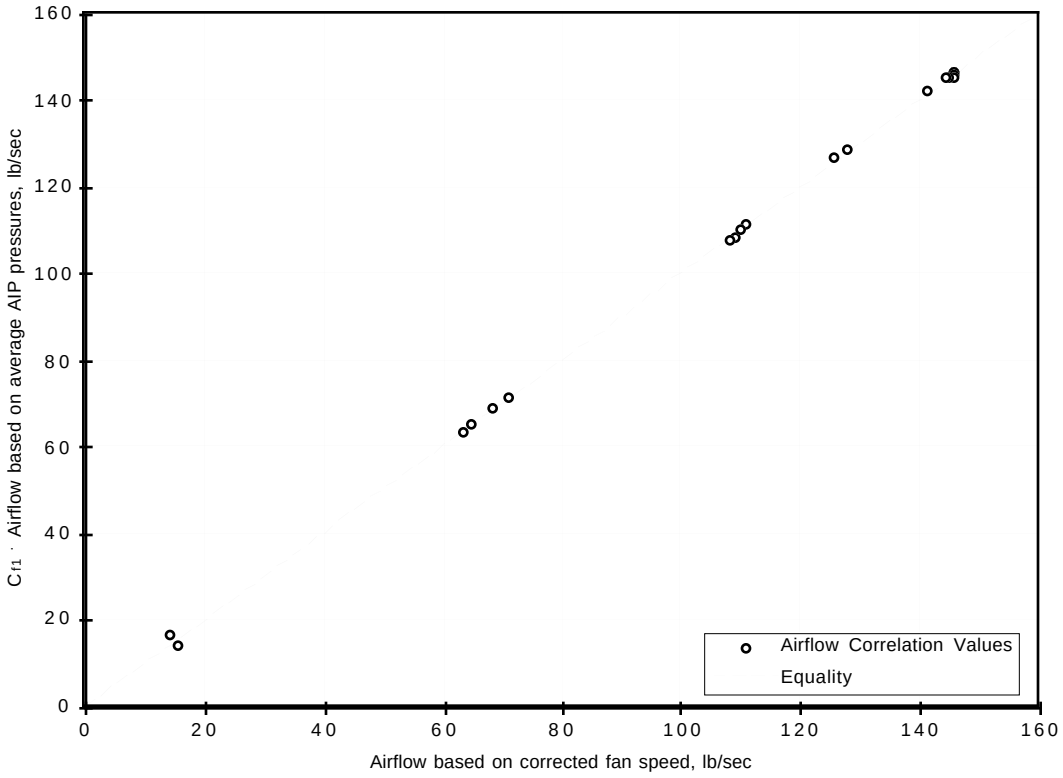

Figure 20. Method 1 calculated airflow as a function of reference method airflow.

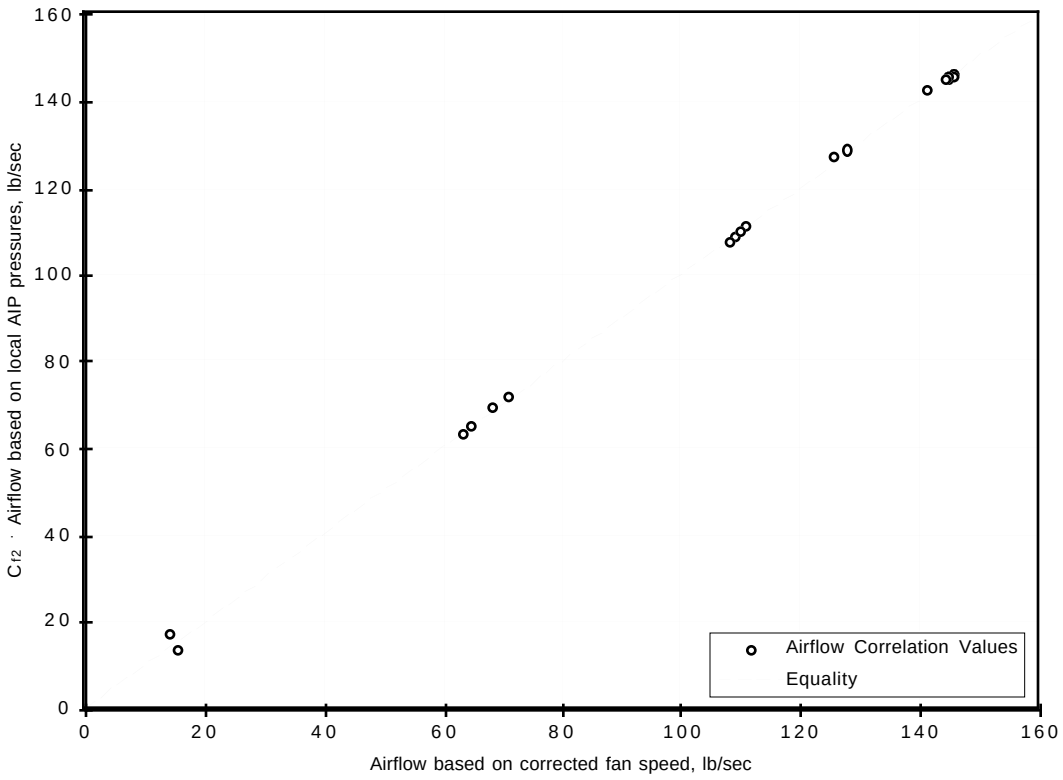

Figure 21. Method 2 calculated airflow as a function of reference method airflow.

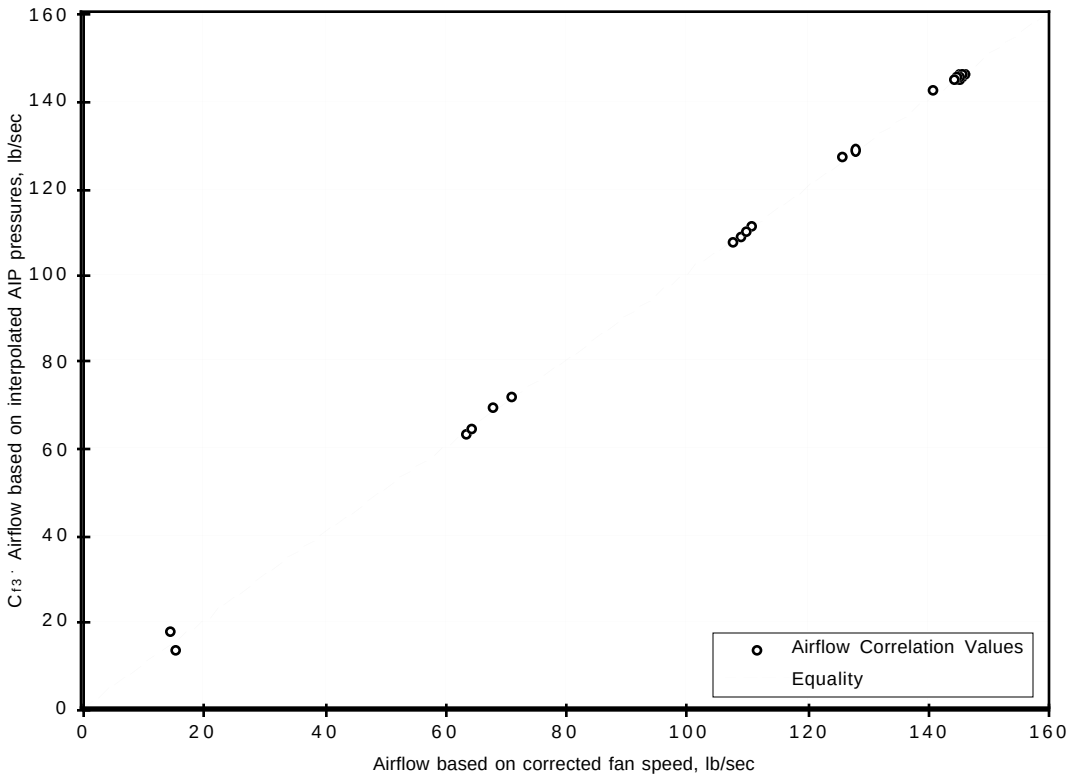

Figure 22. Method 3 calculated airflow as a function of reference method airflow.

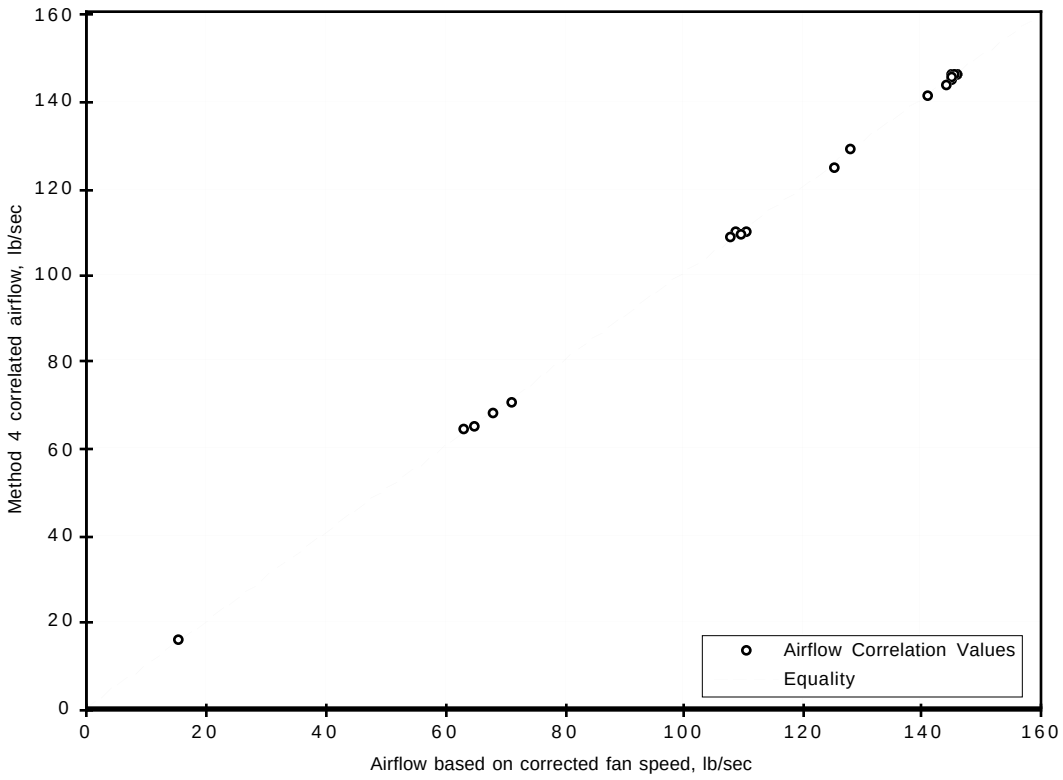

Figure 23. Method 4 calculated airflow as a function of reference method airflow.

in-flight, high-power condition, the Reynolds Number at the AIP is calculated to be 20,000,000. The resulting duct boundary layer thickness (δ) is therefore about 1.3 percent of the duct length. For a duct length of 12 feet this equates to about 1.9 inches. To estimate the quantity of fluid contained within the boundary layer requires knowledge of its profile. The velocity profile is described by the relationship $u/U = (y/\delta)^{1/n}$, where n has the value from 5 to 7 for turbulent flow. The quantity of flow in the boundary layer, and therefore its effect on an estimated flow coefficient can be derived from the boundary layer displacement thickness (δ^*). This has a value of $\delta/(n+1)$. The displacement thickness can be considered as the depth of ideal fluid with no boundary layer passing the same quantity of fluid as that flowing within the actual boundary layer. For a boundary layer depth (δ) of 1.9 inches, the displacement thickness (δ^*) is between 0.2 inches and 0.3 inches. Therefore, the presence of the duct boundary layer effectively reduces the AIP physical flow area by approximately 3.5 to 4.5 percent. Thus, it can be surmised that the combined effects of probe blockage, even though small, and duct wall boundary layer account for about two-thirds of the difference in the derived flow coefficient values from the ideal value of unity.

Another contributing influence could be an error in the assumed AIP physical area and here, was assumed to be 606.21 in^2 based on inlet drawings. An actual measurement was not taken. The in-flight calibration data were taken at temperatures ranging from 425 to 500 °R. An examination of the results shows no distinctive trends which might be a consequence of physical-duct-size variations within this temperature range.

A non-quantifiable influence is the impact of inlet flow distortion and turbulence. A test cell set-up for airflow calibration has extremely low distortion and turbulence levels by intent. Although the distortion levels present at the in-flight calibration conditions were low by in-flight standards, they are significantly higher than those present in a test cell environment.

5.0 AIRFLOW ESTIMATES WITH INLET DISTORTION

With the airflow correlations established for each method, it is now possible to determine the manner in which each method behaves in the presence of high levels of distortion, for as stated in the introduction to this report, the intent is to determine airflow levels to an acceptable level of accuracy when significant levels of distortion are present. Of course, the Reference Method airflow correlation will not change as a result of flow distortion. Thus, it provides a useful reference against which the other methods can be checked for deviations in an effort to understand the impact of inlet distortion on flight airflow estimation methods.

In this section of the report, the range of conditions over which the airflow correlations were studied are presented, engine variable geometry is examined to determine if any changes occurred which might impact the results, and the manner in which each correlation behaved when compared to the Reference Method airflow levels.

5.1 Range of Inlet Conditions

In an effort to assure that the correlations presented in this report have a significant degree of robustness, inlet data that covered a variety of conditions were examined. These conditions covered the 0.3 to 0.4 Mach Number range and altitudes from 20 kft to 35 kft as illustrated by Figure 24. The range of the inlet capture area ratios is from approximately 1.5 to 1.0 as the flight Mach Number ranges from a little less than 0.3 to somewhat in excess of 0.4 as illustrated by the data points of Figure 25. The angle-of-attack and angle-of-sideslip ranges are illustrated by Figure 26. Note that some data points are numbered for reference and correlation with other data in this report and with the total-pressure contour patterns of Figure 30. The ranges of the data in terms of circumferential distortion and radial distortion levels are illustrated by the data of Figure 27. The range of AIP steady-state static-pressure variations and the range of steady-state circumferential distortion variation were from approximately 0 - 0.06 and 0 - 0.12, respectively, as illustrated by Figure 28. The range of AIP turbulence levels and planar wave levels are shown in a combined format in Figure 29. It is felt that these data represent a sufficiently wide range of conditions such that any correlations derived from these analyses will be valid for other inlet configurations and conditions.

This range of conditions produced a variety of steady-state inlet distortion patterns (Figure 30) whose contours are illustrated at M=0.3 at a number of angle-of-attack and angle-of-sideslip conditions except for the AOA=-10.3, AOSS=0.2 contours which were obtained at M=0.4. Note that these distortion patterns are numbered for reference purposes and correspond to the numbered points on Figures 26-29.

5.2 Engine-Operation Tracking

As was done when establishing the Reference Method airflow calibration during the ground test phase, engine control schedules were examined to determine if they deviated from the clean inlet flow schedules that were previously determined. Interrogation of these parameters revealed that engine operation did not shift as a result of the distorted inlet conditions. As an example, fan variable geometry tracking for ground-test, flow-correlation, and stabilized aerodynamic attitude conditions is shown in Figure 31.

5.3 Average Wall-Static-Pressure and Average Total-Pressure Derived Airflow (Method 1)

The deviation between the Method 1 estimated airflow and the Reference Method airflow is shown plotted in Figure 32 as the percent difference between the Method 1 airflow and the Reference Method

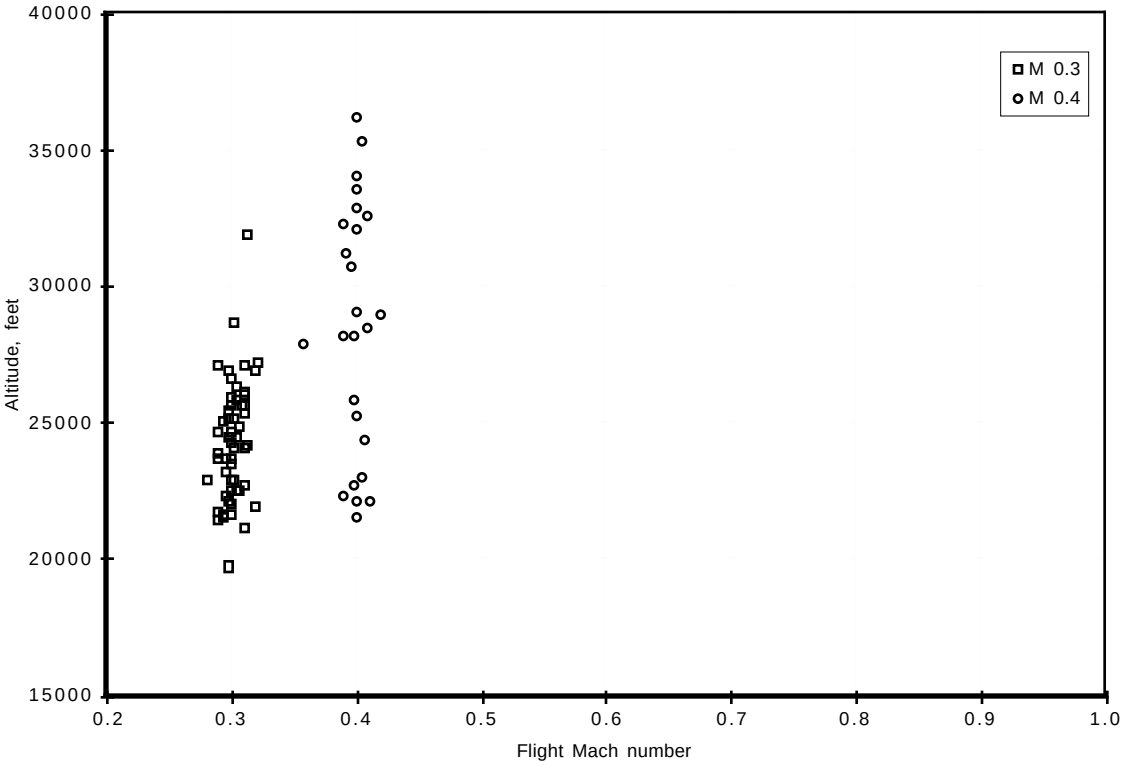

Figure 24. Test range of Mach numbers and altitudes.

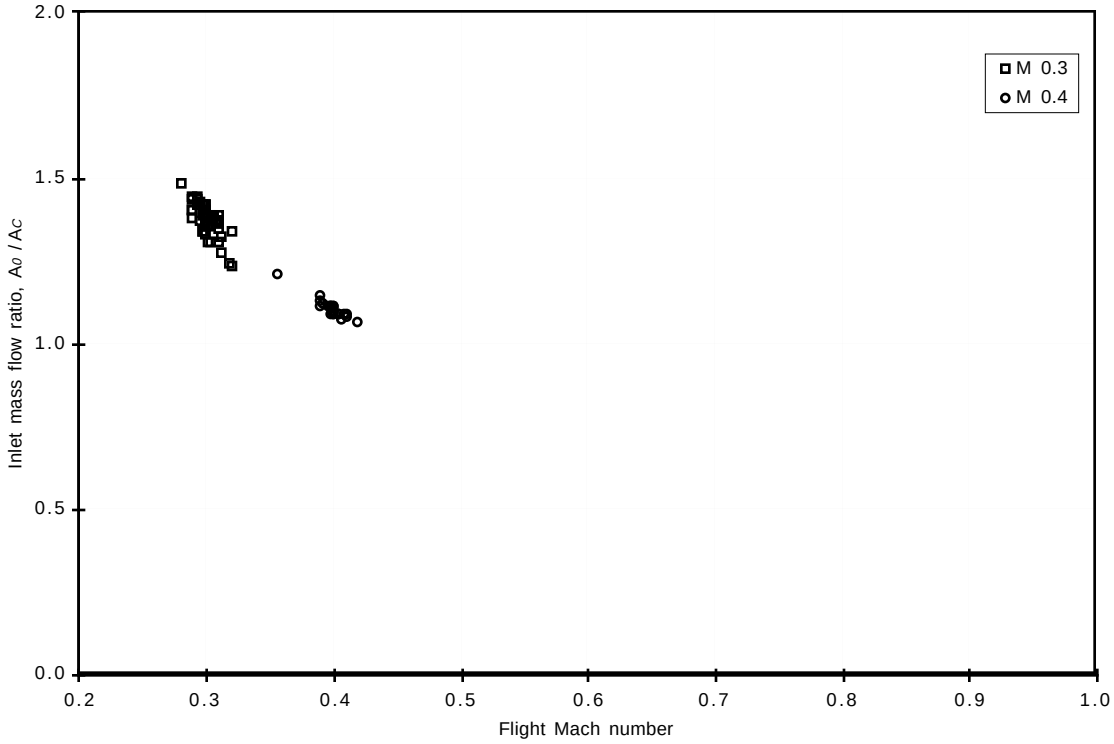

Figure 25. Test range of inlet capture area ratios.

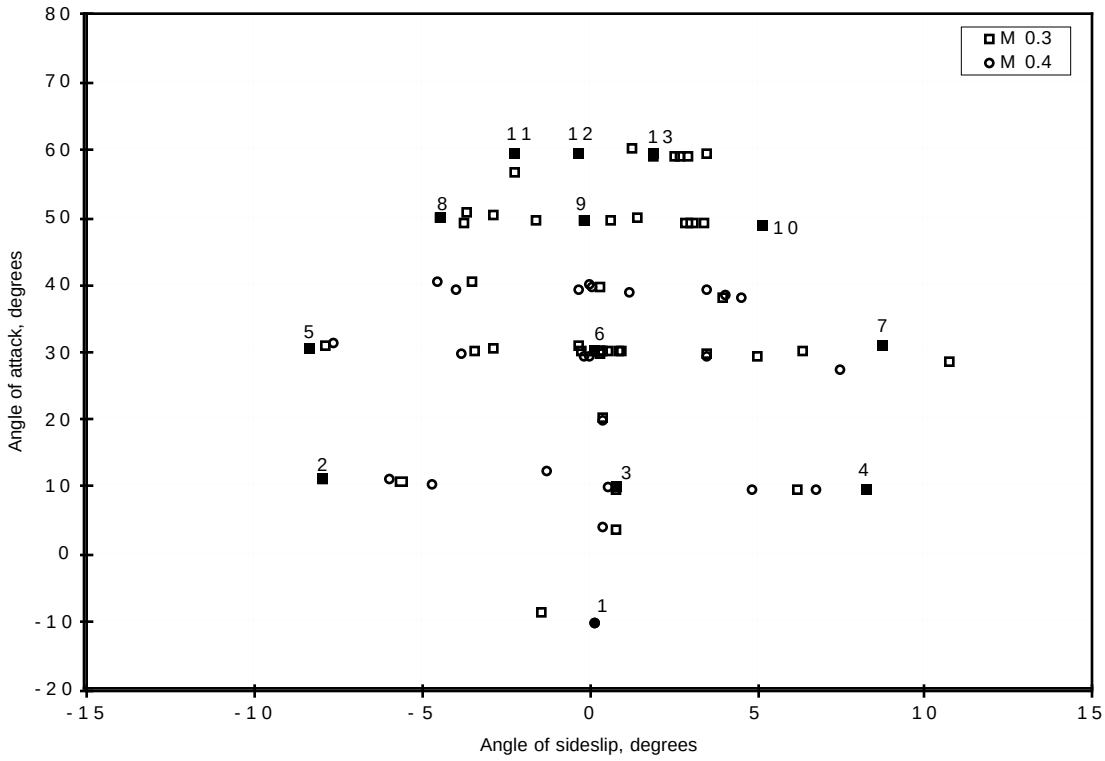

Figure 26. Test range of inlet data maneuver conditions.

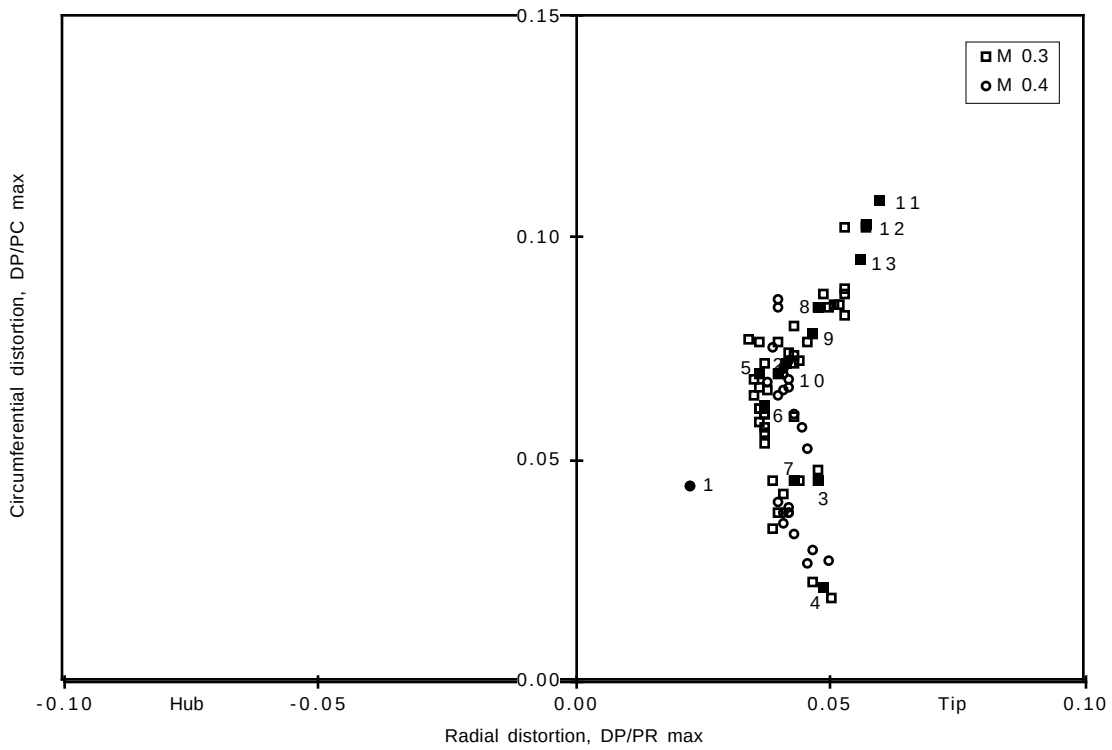

Figure 27. Test range of steady-state circumferential and radial distortions.

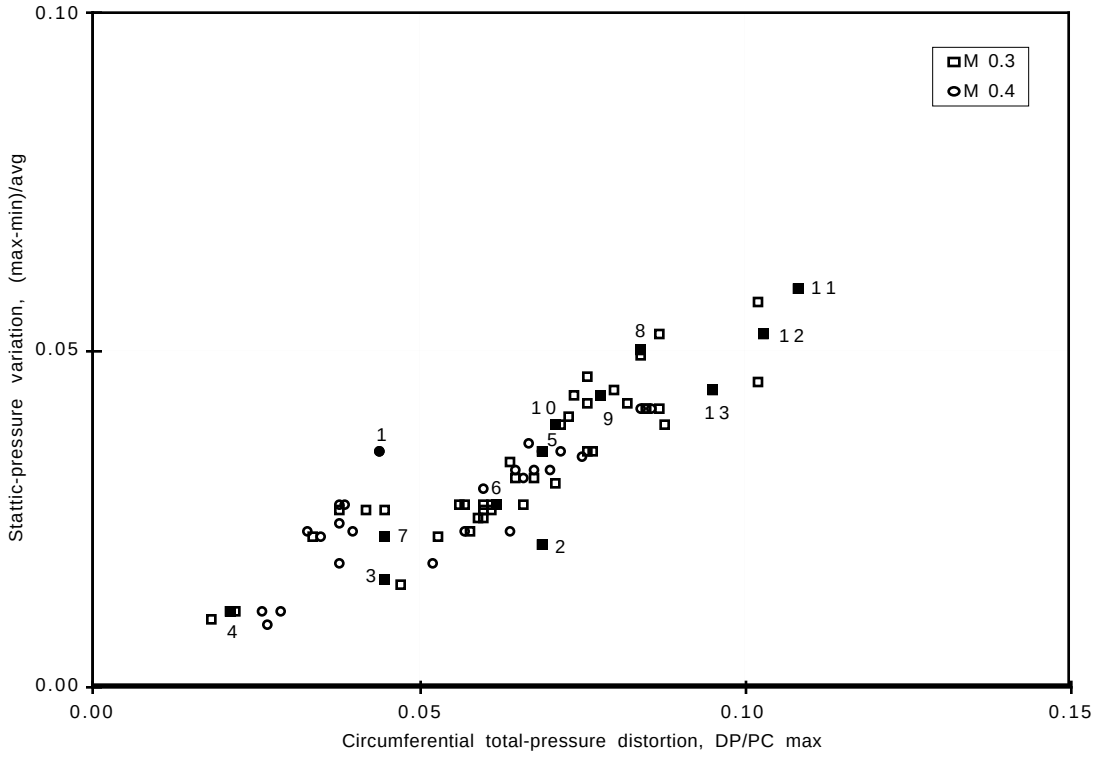

Figure 28. Test range of AIP static-pressure variations and steady-state circumferential distortions.

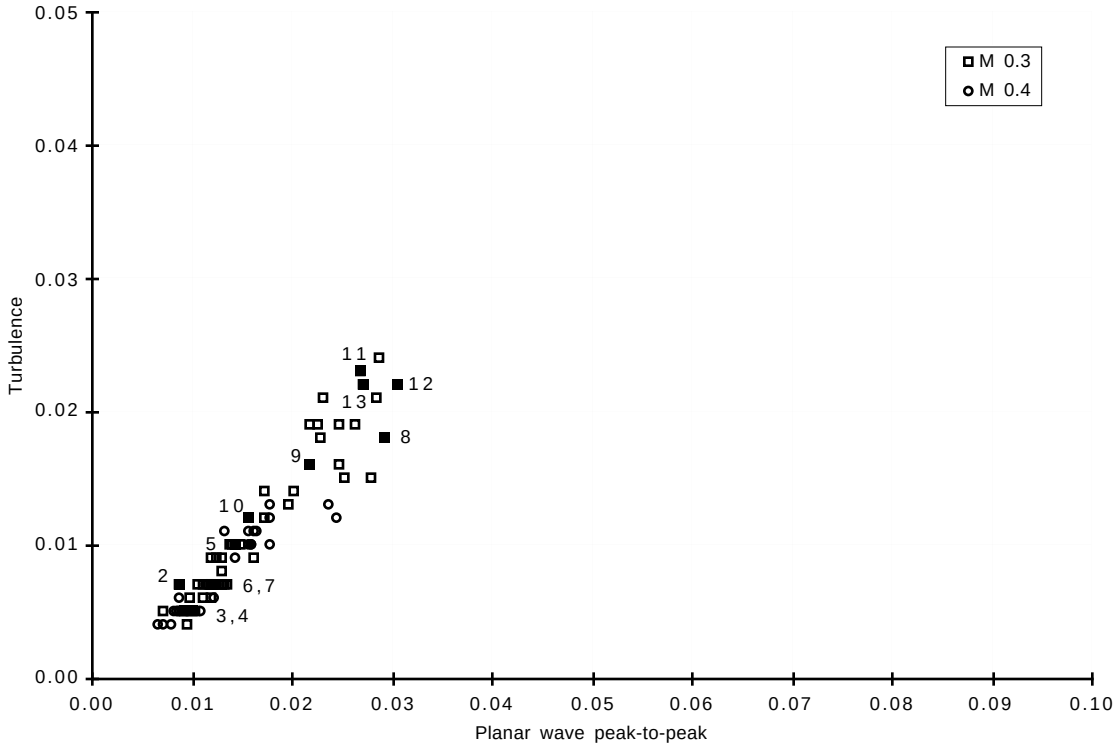

Figure 29. Test range of turbulence and planar wave levels.

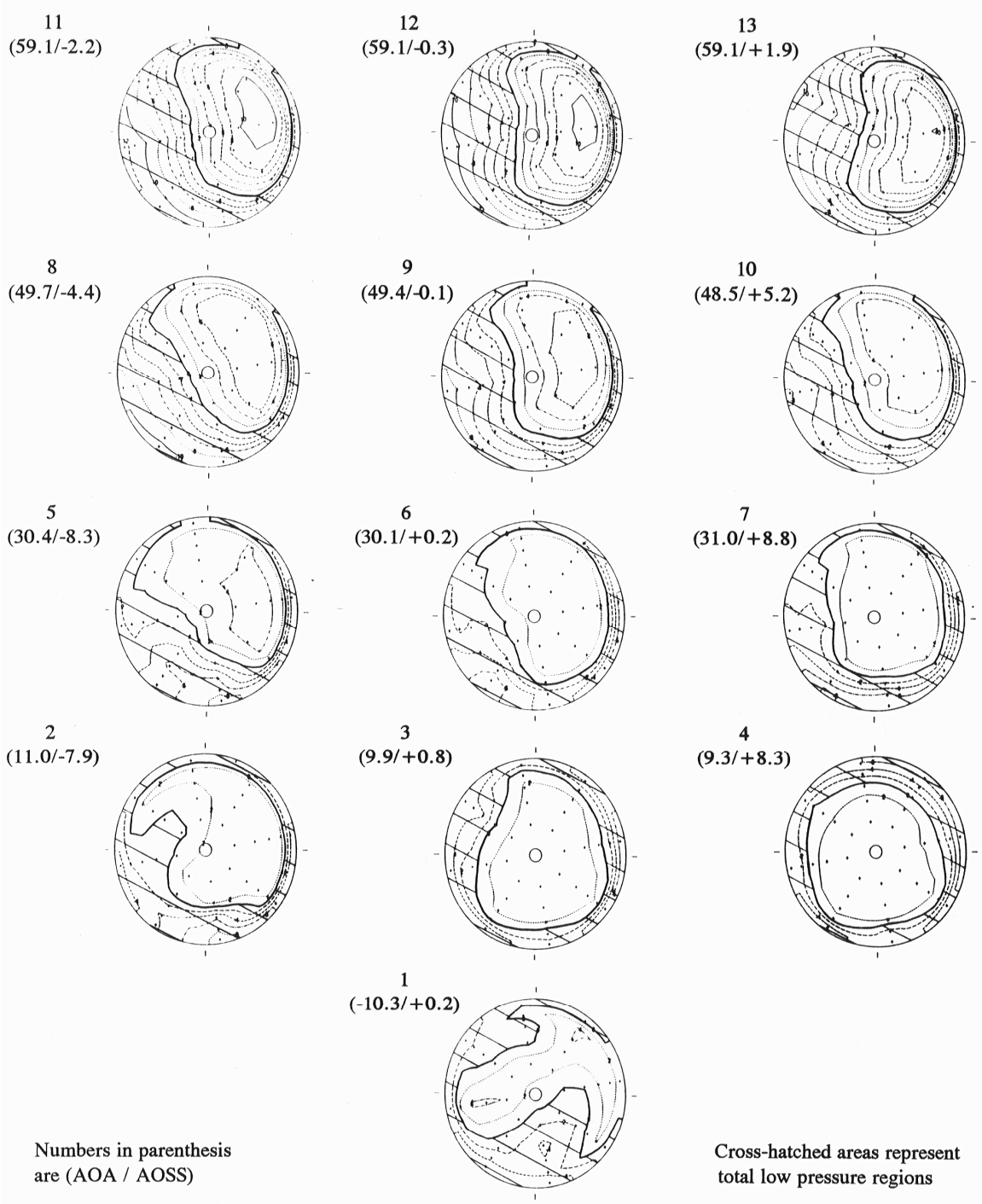

Figure 30. Right inlet (ALF) steady-state AIP total-pressure patterns for a range of fixed aerodynamic attitude conditions.

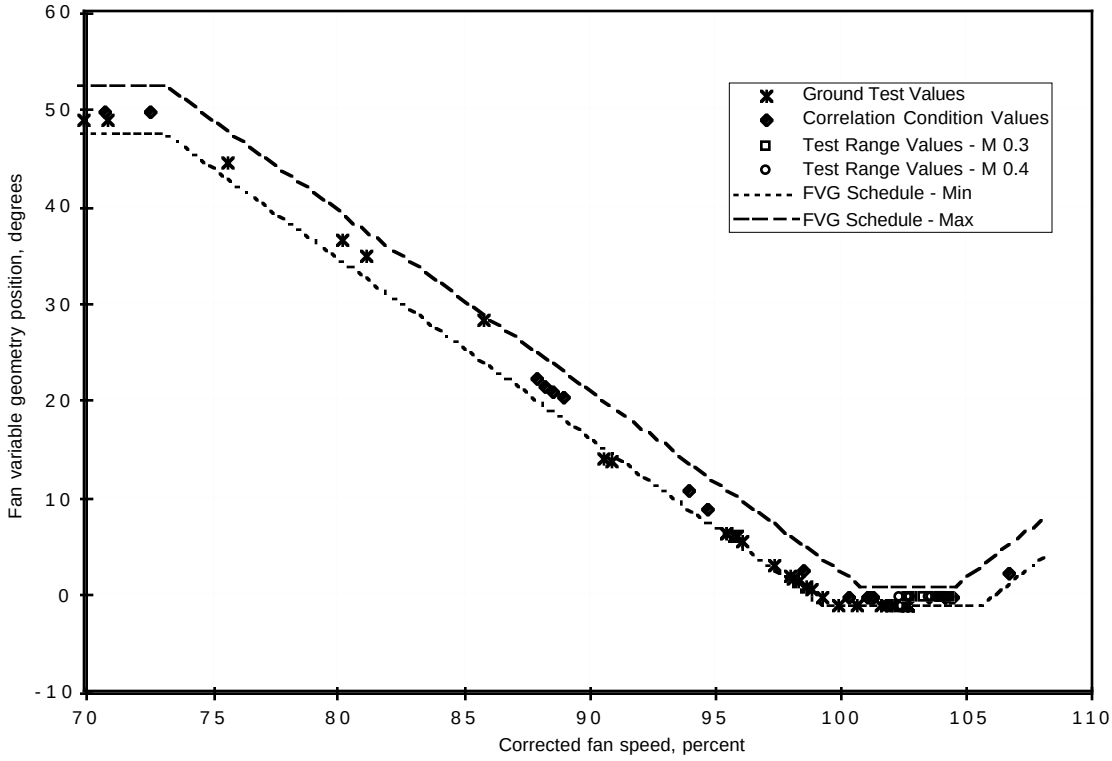

Figure 31. Fan variable geometry tracking for ground test, correlation, and fixed aerodynamic attitude conditions.

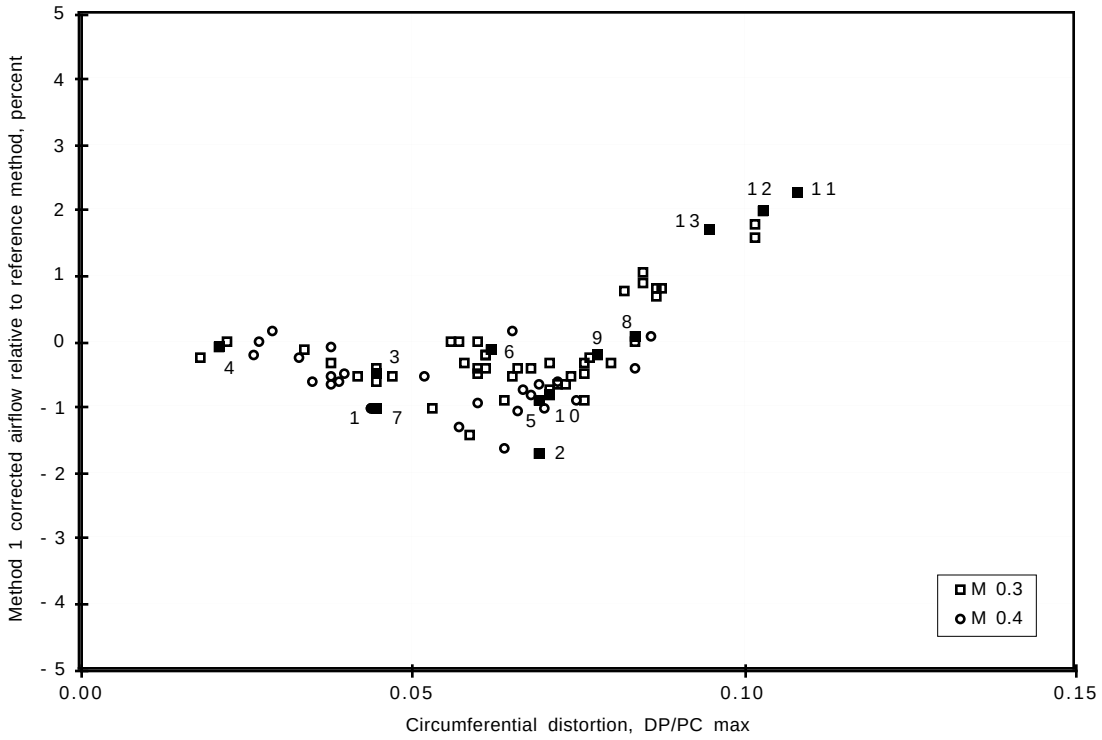

Figure 32. Method 1 corrected airflow relative to reference method as a function of circumferential distortion level.

airflow nondimensionalized by the Reference Method airflow. The figure shows that the Method 1 airflow estimation technique tends to underestimate the airflow with respect to the Reference Method airflow for all except the highest steady-state distortion levels (DP/PC> ~0.08). The spread in these data has a range of 4.0 percent (maximum of 2.2 percent and a minimum of -1.8 percent).

5.4 Estimated Rake-Average Static-Pressures and Individual Probe Total-Pressures Derived Airflow (Method 2)

The deviation between the Method 2 estimated airflow and the Reference Method airflow is shown plotted in Figure 33 as the percent difference between the Method 2 airflow and the Reference Method airflow nondimensionalized by the Reference Method airflow. The figure shows that the Method 2 airflow estimation technique tends to reproduce or underestimate the airflow with respect to the Reference Method airflow for the range of steady-state levels of distortion encountered. The spread in these data is considerably reduced from the spread of Method 1 with the spread being approximately 2.3 percent (maximum of 0.3 percent and a minimum of -2.0 percent).

5.5 Estimated Individual Probe Static-Pressures and Individual Probe Total-Pressures Derived Airflow (Method 3)

The deviation between the Method 3 estimated airflow and the Reference Method airflow is shown plotted in Figure 34 as the percent difference between the Method 3 airflow and the Reference Method airflow nondimensionalized by the Reference Method airflow. The results are very similar to the Method 2 results with the spread being approximately 2.3 percent (maximum of 0.2 percent and a minimum of -2.1 percent).

5.6 Fan Discharge Average Static-Pressure and AIP Average Total-Pressure Derived Airflow (Method 4)

The deviation between the Method 4 estimated airflow and the Reference Method airflow is shown plotted in Figure 35 as the percent difference between the Method 4 airflow estimated at the measured pressure ratio and the Reference Method airflow nondimensionalized by the Reference Method airflow. The results tend to correlate well with the Reference Method airflow with the spread being approximately 0.6 percent (maximum of 0.3 percent and a minimum of -0.3 percent).

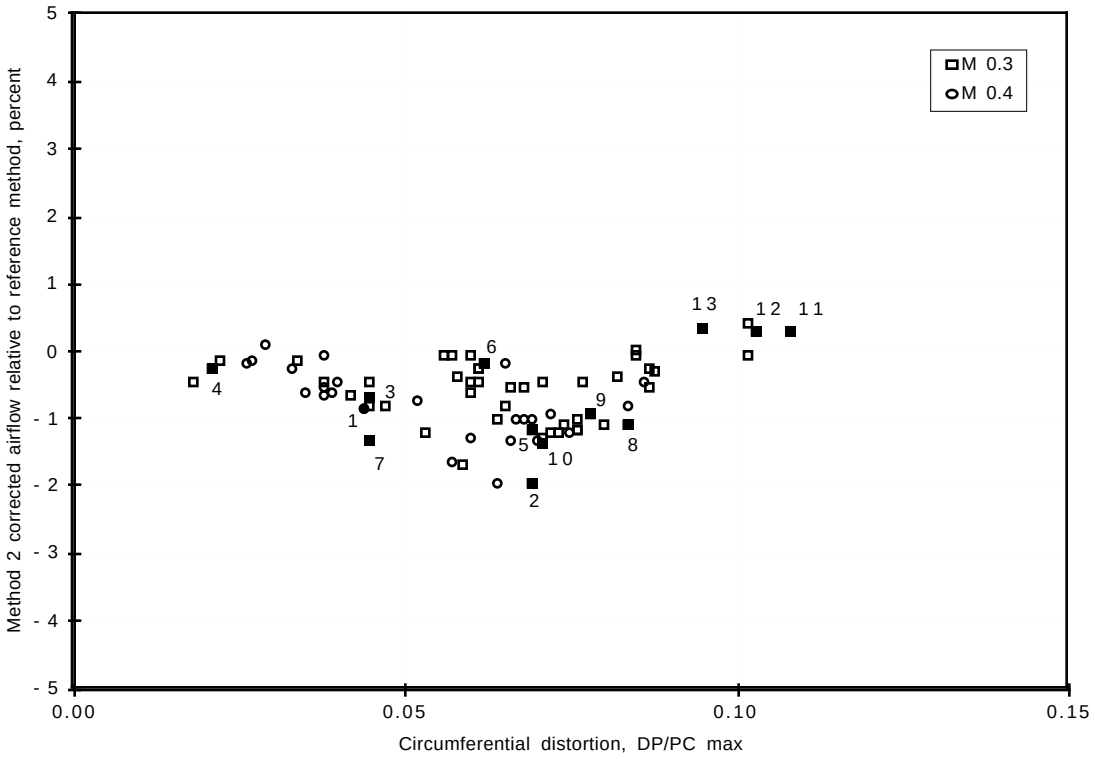

Figure 33. Method 2 corrected airflow relative to refernce method as a function of circumferential distortion level.

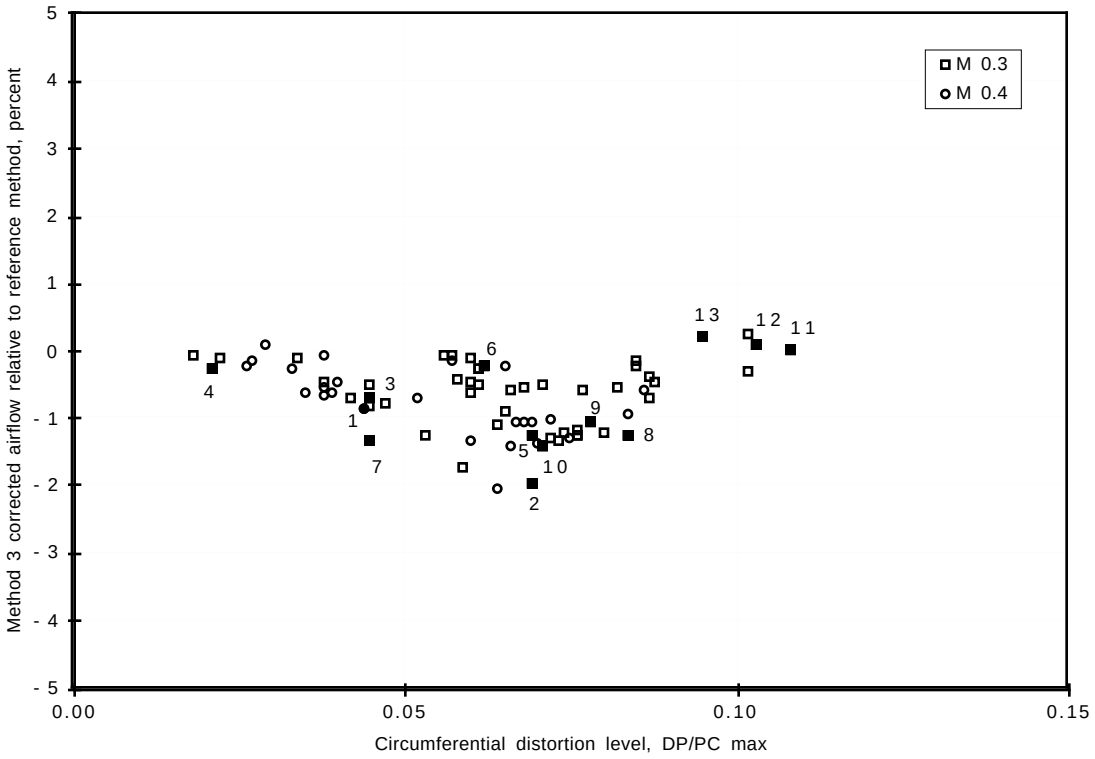

Figure 34. Method 3 corrected airflow relative to reference method as a function of circumferential distortion level.

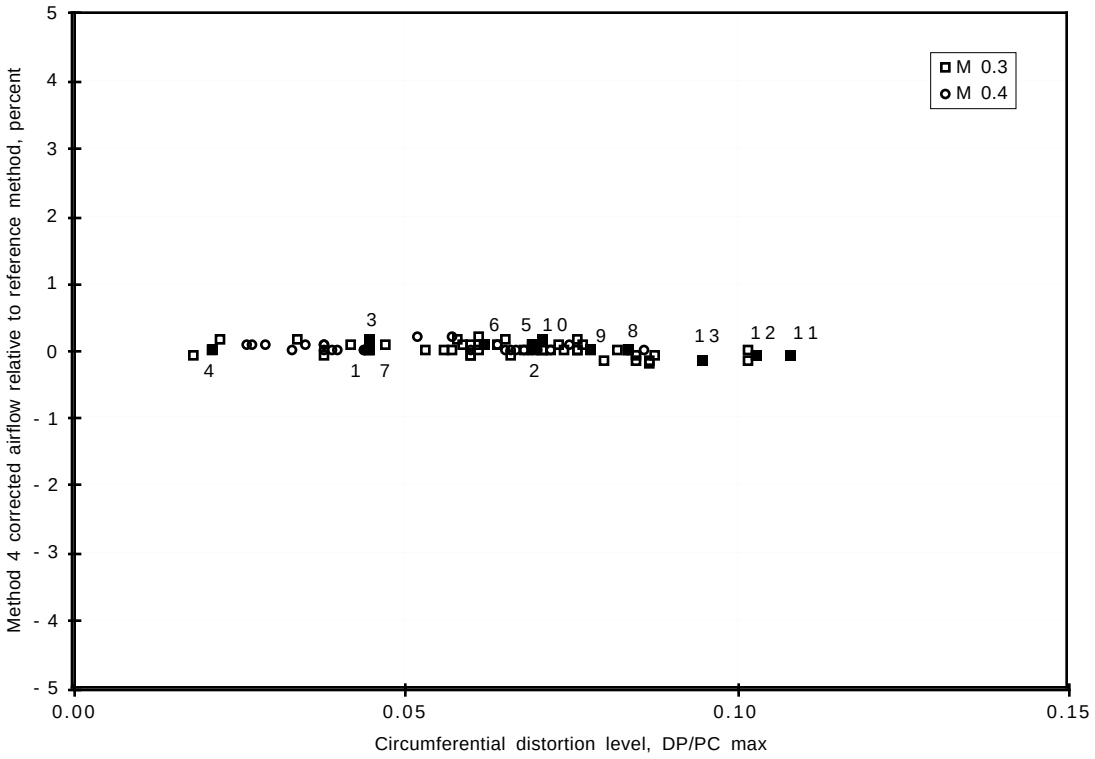

Figure 35. Method 4 corrected airflow relative to reference method as a function of circumferential distortion level.

6.0 DISCUSSION OF RESULTS

Examination of the results of Section 5.0 provides significant insight to the efforts required to establish acceptable estimates of airflow in the presence of significantly distorted inlet flows. These results are discussed in the following paragraphs.

Comparison of the Method 1 airflow correlation (Figure 32) with the Method 2 airflow correlation (Figure 33) shows that calculating airflows on a per probe, equal area basis provides an estimate of airflow that has significantly less deviation from the Reference Method airflow than calculating flows based on AIP average static- and total pressures. Interestingly, when an attempt is made to provide a better estimate of the local static pressure associated with each total-pressure probe (Figure 34), essentially no gain in correlation accuracy is achieved relative to using a rake average static pressure. Further, interrogation of Figures 32 through 34 provides no discernible trends when examined by Mach Number, angle of attack, and/or angle of sideslip.

Of significant interest are the results obtained by taking the static-pressure measurements downstream of the fan in an effort to take advantage of the attenuation of inlet distortion through the fan. As Figure 35 clearly illustrates, the correlation shows little deviation from the Reference Method airflow levels and hence, clearly no effect of inlet distortion on the calculated airflow levels.

The visual comparisons of the airflow estimation methods as discussed in Section 5.0 can be quantified using standard statistical techniques. The systematic and random errors have been calculated and are presented in Table 7 for each of the airflow estimation methods expressed as a percentage of the airflow at high power (145.8 lbm/sec).

Table 7. Systematic and random errors of airflow estimation techniques.

Method	Systematic Error	Random Error
1	-0.26%	±0.77%
2	-0.67	±0.53
3	-0.71	±0.52
4	0.02	±0.08

Examination of the table shows that when the related Methods 1, 2, and 3 are compared, they all underestimate the airflow as indicated by the negative systematic error, but that Method 1 underestimates the airflow by the least amount. Methods 2 and 3 of these related methods result in essentially equivalent and smaller random errors. Method 4 shows that this airflow estimation technique has essentially no systematic error or random error.

When these previous results are examined as a combined set, another finding can be inferred as follows: Given that: 1) careful use of the AIP static-pressure and total-pressure data provides results with a small spread, 2) all results show no discernible trends with distortion level (radial or circumferential) or turbulence level, and 3) Method 4 provides results equivalent to the Reference Method, one can deduce that the Reference Method (flow-speed correlation) will provide the most accurate estimate of airflow for the ranges of the inlet conditions examined in this study.

These results, that is, the inferred accuracy of the Reference Method as well as the small systematic errors for Methods 1-4 were unexpected. Knowledgeable industry investigators had long expected to find trends (systematic errors) in airflow that correlated with the level of distortion and/or the unsteadiness of the inlet flow. To gain an independent perspective of the HARV results, the relative levels of airflow-at-speed measured during the F404 Fan Rig testing with inlet distortion screens were examined. These distortion screens, which provided time-averaged (steady-state) values of circumferential distortion ranging essentially from zero to approximately 0.17 and radial distortion values ranging from 0.06 tip to 0.06 hub, covered a significantly broader range of distortion levels than produced by the HARV inlet. These fan rig data, which consisted of fan map pressure ratio - corrected flow representations at 100 percent corrected speed for thirteen distortion screens, were correlated (on the same operating line) to examine the change in flow pumping associated with inlet distortion (relative to a clean inlet flow condition) as a function of time-averaged circumferential and radial distortion levels. Based on this work, the HARV inlet distortion levels (circumferential from 0.02 to 0.12 and tip radial from 0.03 to 0.06) would be expected to show a variation in airflow pumping ranging from approximately 0.4 percent for the lowest distortion condition to 0.9 percent for the largest distortions - implying that a potential flow spread of 0.5 percent may be anticipated for the HARV results given the range of distorted inlet flow conditions. This variation is similar in magnitude to the measured errors in the Methods 1, 2, and 3 correlation results (see Table 7). Therefore, no significant trends in the HARV results would be expected which may be attributed to the influence of time-averaged inlet distortion.

A consequence of the time-averaged distortions having no significant impact, is that it can be deduced that turbulence has little or no impact . Thus, the flow pumping capacity of the F404-GE-400 fan also is not affected by levels of turbulence up to approximately 2.4 percent produced by the HARV inlet.

The Methods 1, 2, and 3 data (Figures 32 - 34) cause an investigator to ask if the deviations from the Reference Method can be attributed to, or correlated with, characteristics associated with the distortion patterns (Figure 30). The only positive finding, as previously stated in this section, indicates that providing an estimate of the static pressure associated with each total-pressure probe will reduce the positive deviations associated with the high levels of steady-state circumferential distortion ($\Delta P/PC \geq 0.09$) and turbulence ($Tu \geq 0.02$).

An investigator might expect that the negative bias seen in Methods 2 and 3 might be attributable to features of the flow. Correlations with circumferential distortion, radial distortion, the absolute magnitude of combined circumferential distortion and radial distortion, turbulence levels, turbulence levels and circumferential distortion, the maximum circumferential-distortion to maximum radial- distortion ratio, and quantification of distortion profile characteristics (circumferential distortion and radial distortion plotted as a function of ring immersion at the AIP) including calculating circumferential distortion and radial distortion gradient parameters were attempted. None of the methods resulted in explanations as to why the deviation relative to the Reference Method would be worst for Pattern No. 2 followed by patterns No. 5, 10, 7, 8 , 1, 9, 3, 4, 13, 12, 6, and 11 in order of decreasing deviation (absolute magnitude).

The Method 4 results (Figure 25) were examined in significant detail to assure that the findings were not the result of an unapparent “identity” relationship. First it was determined that the engine control scheduling was the same during the distorted inlet flight conditions as during the correlation flight conditions by examining both physical fan speed as a function of corrected inlet temperature and corrected turbine temperature as a function of corrected inlet temperature. Then, it was established that the fan discharge static pressure to fan inlet total pressure ratio - fan corrected speed relationship was unchanged between the correlation conditions and the distorted inlet flight conditions. Thus, there is every reason to believe the results are as good as they imply. However, the data all fall at a pressure ratio of 3.5 or greater and are on the flat part of the correlation (Figure 19). This will have a tendency to reduce the spread in the data. Part power data are needed to assure the robustness of Method 4.

7.0 CONCLUSIONS AND RECOMMENDATIONS

The high quality of the data obtained as part of the HARV propulsion research efforts has allowed calculations to be made that provide significant insight into making measurements that lead to estimates of airflow with accuracies far exceeding those previously obtained in flight, even in the presence of significant levels of inlet distortion. Achievement of these types of accuracy is attributed to the attention given to: 1) the instrumentation, data acquisition, data recording, and data reduction systems, 2) the development of the flow-speed calibration during a ground test for the flight engine, and 3) the establishment of in-flight, low-distortion flow correlations.

As a result of these efforts and the subsequent analyses, it is concluded that:

1. It is possible to estimate the magnitude of the airflow in the presence of inlet distortion to within a spread of 2.3 percent and a systematic error of approximately -0.7 percent using only AIP static-pressure and total-pressure instrumentation (Methods 2 and 3) if proper attention is paid to calibration and correlation efforts.

2. Taking advantage of fan distortion attenuation, use of fan-discharge wall-static pressures and the AIP total pressures will allow obtaining the magnitude of the airflow in the presence of inlet distortion to within a spread of 0.6 percent with essentially no systematic error, again with paying proper attention to the calibration and correlation efforts. It should be noted that this method requires that engine control scheduling give rise to a unique fan operating line as a function of fan corrected speed. Some control schemes will not result in such a unique relationship and hence, will invalidate this method.

3. The results of this study show that flow unsteadiness for turbulence levels of up to approximately 2.4 percent have no impact on the flow pumping capacity of the F404-GE-400 fan.

4. A calibrated flow-speed correlation appears to provide the most accurate estimate of airflow in the presence of inlet distortion as compared to all the airflow methods that were investigated. Coincidentally, this method requires the least instrumentation.

If an investigator is interested in estimating airflow in flight using methods other than the flow-speed correlation, it is recommended that the methods of this report be followed. In this manner, it will be possible to obtain accuracies comparable to those obtained in the investigation reported herein. Specifically, one should conduct a ground test of the engine using a correlated bellmouth to obtain the Reference flow-speed calibration. Then, other flow correlation methods can be established at low distortion inlet conditions such as 1-g flight with capture area ratios less than unity.

While the results of this study are very encouraging, they must be tempered with the realization that, while encompassing a broad range of circumferential distortion levels and a range of moderate turbulence levels, the range of radial distortions encountered was quite low and all had tip-radial distortion content. Thus, it is recommended that a similar study such as this one be conducted for an inlet-engine combination where the inlet distortions might range from hub-radial to tip-radial distortion patterns and the fan component of the engine might have speed lines with more slope than the F404-GE-400 fan. Further, including part power settings, in addition to power settings where the engine airflow is a maximum, would provide the data necessary to give a broader validation to the conclusions reached in this study.

ACKNOWLEDGMENTS

The authors want to recognize the expertise, diligence, and support provided by the NASA Dryden Flight Research Center HARV Team. It is a direct result of their efforts that high quality inlet data were acquired and that made possible the research efforts reported herein.

Further, the efforts of Mr. J. McFadyen in obtaining the static test-cell data and providing the ground corrected flow-corrected speed calibration and associated results are worthy of special mention, for it is upon these results that all of the analyses in this report rest.

Special thanks are due Ms. P. Shivers for her assistance in establishing the special data handling and processing techniques, and in the preparation of this report.

The efforts of Mr. K. Walsh of the NASA Dryden Flight Research propulsion team, in preparing the electronic version of this report, is greatly appreciated.

APPENDIX A - EQUATIONS

The detailed equations and relationships are recorded in this appendix for reference purposes.

A1. Capture Area Ratio

The capture area ratio is defined as the area, A_O, associated with the stream tube containing the flow entering the inlet divided by the inlet physical "capture" area, A_C, as illustrated by the following diagram.

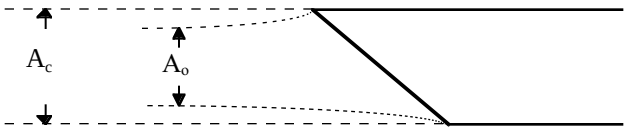

Beginning with the continuity equation, the following relationship for A_O can be written as:

$$A_o = W_o/(\rho_o V_o)$$

From the definitions of a thermally and calorically perfect gas, corrected flow conditions, inlet recovery for an adiabatic flow, and the isentropic Mach number relationships, the following relationship can be readily derived relating A_O to the free stream Mach number, inlet recovery, and engine corrected airflow. Dividing by the capture area, A_C, results in the following expression for the capture area ratio.

$$A_o/A_c = (1/FF)\cdot W_{ceng}\cdot\eta\cdot\left(\sqrt{T_{Std}}/P_{Std}\right)\cdot(1/A_c) \tag{A1}$$

where FF is the flow function parameter. It is a function of Mach number alone and is defined as

$$FF = \left(W\sqrt{T_t}\right)/(P_t A) = \sqrt{g_c\gamma/R}\cdot M\cdot\left[1+(\gamma-1)/2\cdot M^2\right]^{-(\gamma+1)/(2\cdot(\gamma-1))} \tag{A2}$$

A2. Flow Relations

Because static- and total-pressure measurements are being used in the flow calculations, it is convenient to write the flow function $W\sqrt{T_t}/(P_t A)$ in terms of the static-pressure to total-pressure ratio rather than Mach number as in Equation A2. Making use of the isentropic relationship

$$P_s/P_t = \left[1+(\gamma-1)/2\cdot M^2\right]^{-\gamma(\gamma-1)}$$

Equation A2 can be written as

$$W\sqrt{T_t}\Big/(P_t A) = \left\{2g_c\gamma/\left[R(\gamma-1)\right]\right\}^{1/2}\cdot\left[\left(P_s/P_t\right)^{(1-\gamma)/\gamma}-1\right]^{1/2}\cdot\left(P_s/P_t\right)^{(1+\gamma)/2\gamma} \tag{A3}$$

In the above form, the equation can be applied to duct average quantities to obtain the flow for Method 1 airflow correlation or by summing the local flow functions in the following manner for Methods 2 and 3 airflow correlations.

$$W\sqrt{T_t}/(P_t A) = \sum\left[W\sqrt{T_t}/(P_t A)\right]_i\cdot A_i/A \tag{A4}$$

A3. Inlet Flow Descriptor Definitions

For a given pattern of 40 total-pressure measurements (8 rakes, 5 rings), the total-pressure distortion descriptors are defined as follows:

Maximum Circumferential Distortion Descriptor - DP/PC max

This circumferential ring pressure distortion index is based on the calculation of $DP/PC_{ring\ i}$,

where the subscript "ring i" refers to any of the five pressure rings.

The rings are counted in ascending order, innermost to outermost.

$$DP/PC_{ring\ i} = \{[\ PAV_{ring\ i} - PMIN_{ring\ i}\ ] / PAV\} \quad \text{for rings } i=1,5$$

where:

1. $PAV_{ring\ i}$ = area-averaged total pressure of ring i
2. $PMIN_{ring\ i}$ = minimum total pressure in the largest low pressure region in ring i
3. PAV = area-averaged total pressure over the complete face

DP/PC max is defined as the largest of:

$$0.5 \cdot [DP/PC_{ring\ i} + DP/PC_{ring\ i+1}] \qquad \text{for } i=1,4 \qquad \text{(A5)}$$

Maximum Radial Distortion Descriptor - DP/PR max

Similar to DP/PC, DP/PR is calculated for each of the five rings as follows:

$$DP/PR_{ring\ i} = [\ PAV - PAV_{ring\ i}\ ] / PAV \quad \text{for rings } i=1,5 \qquad \text{(A6)}$$

where:

1. PAV = area-averaged total pressure over the complete face
2. $PAV_{ring\ i}$ = area-averaged total pressure of ring i

If a DP/PR_{ring} value is negative, it is assumed to be zero.

DP/PR max is defined as the larger of $DP/PR_{ring\ 1}$ or $DP/PR_{ring\ 5}$

If DP/PR max is located in ring 1, the distortion is hub radial.

If DP/PR max is located in ring 5, the distortion is tip radial.

Planar Wave Peak-to-Peak

The steadiness of the inlet recovery with time is quantified by the planar wave peak-to-peak parameter. Thus, the AIP average total pressure is computed at each time slice over a time period of interest. Then, the maximum value minus the minimum value in this time period divided by the average AIP total pressure is defined as the planar wave peak-to-peak value. It can be expressed in equation form as

$$\hat{P}_t(k) = 1/N \sum_{i=1}^{N} P_{ti}(k)$$

where N denotes the number of total-pressure probes.

$$\text{Planar Wave Peak-to-Peak} = [\text{Max } \hat{P}_t(k) - \text{Min } \hat{P}_t(k)]/\overline{P}_t \tag{A7}$$

where $\hat{P}_t(k)$ is the spatial average of the total pressures at the AIP and $\overline{P}_t$ is the time-averaged value of the spatial averages, that is,

$$\overline{P}_t = 1/M \cdot \sum_{k=1}^{M} \hat{P}_t(k) \tag{A8}$$

where M denotes the number of scans in the data sample.

Turbulence - Tu

The inlet turbulence parameter is the average of the root-mean-square of the total-pressure fluctuations at each AIP high-response total-pressure probe divided by the time-averaged total pressure of the probe.

$$Tu = 1/N \cdot \sum_{i=1}^{N} \left\{ 1/M \cdot \sum_{k=1}^{M} \left[\left(P_{ti}(k) - \overline{P}_{ti} \right) / \overline{P}_{ti} \right]^2 \right\}^{1/2} \tag{A9}$$

where N is the number of total-pressure probes included in the average and M denotes the number of scans in the data sample.

APPENDIX B - INLET TEMPERATURE ANALYSIS

The accurate measurement of engine inlet temperature required special consideration. The calculation of engine corrected airflow or fan corrected speed required engine inlet total temperature as an input. Typically, it can be obtained from either the aircraft total-temperature sensor or the engine fan-inlet total-temperature sensor. The known attributes of these measurements precluded using either one without additional analysis.

The aircraft production-probe sensor used to measure freestream total temperature is located beneath the cockpit on the bottom of the fuselage. At straight and level flight conditions, it has an accuracy of ±1 ^{o}R. At high angle of attack conditions (AOA> 20 degrees), this probe becomes significantly biased due to the probe being misaligned with the freestream flow. Figure B1 illustrates this latter point quite dramatically since it illustrates the significant deviation of the aircraft temperature probe (TTMPR) from both the left (T1LR) and right (T1RR) engine inlet temperature probes. Note that the deviation of the flight temperature probe correlates with the change in angle of attack (ALPHAL).

The engine inlet temperature measurement, located between the struts of the inlet guide vanes, has an accuracy of ±2 ^{o}R. It was observed during ground testing that the sensor has a bias when compared to the more accurate test stand sources. In order to obtain an accurate total temperature from low to high angle of attack, the engine sensor was used since it did not seem to be biased by high angle of attack. However, the engine inlet temperature measurement has a bias correction applied to it based on the aircraft sensor. This bias was calculated through a comparison to the aircraft production probe sensor at low angle of attack.

This comparison determined that a -3 ^{o}R bias (Figure B2) would be applied to the engine temperature to make it equivalent to the freestream measurement. This study was performed on a data set of 74 stabilized conditions at low angle of attack and high engine airflow.

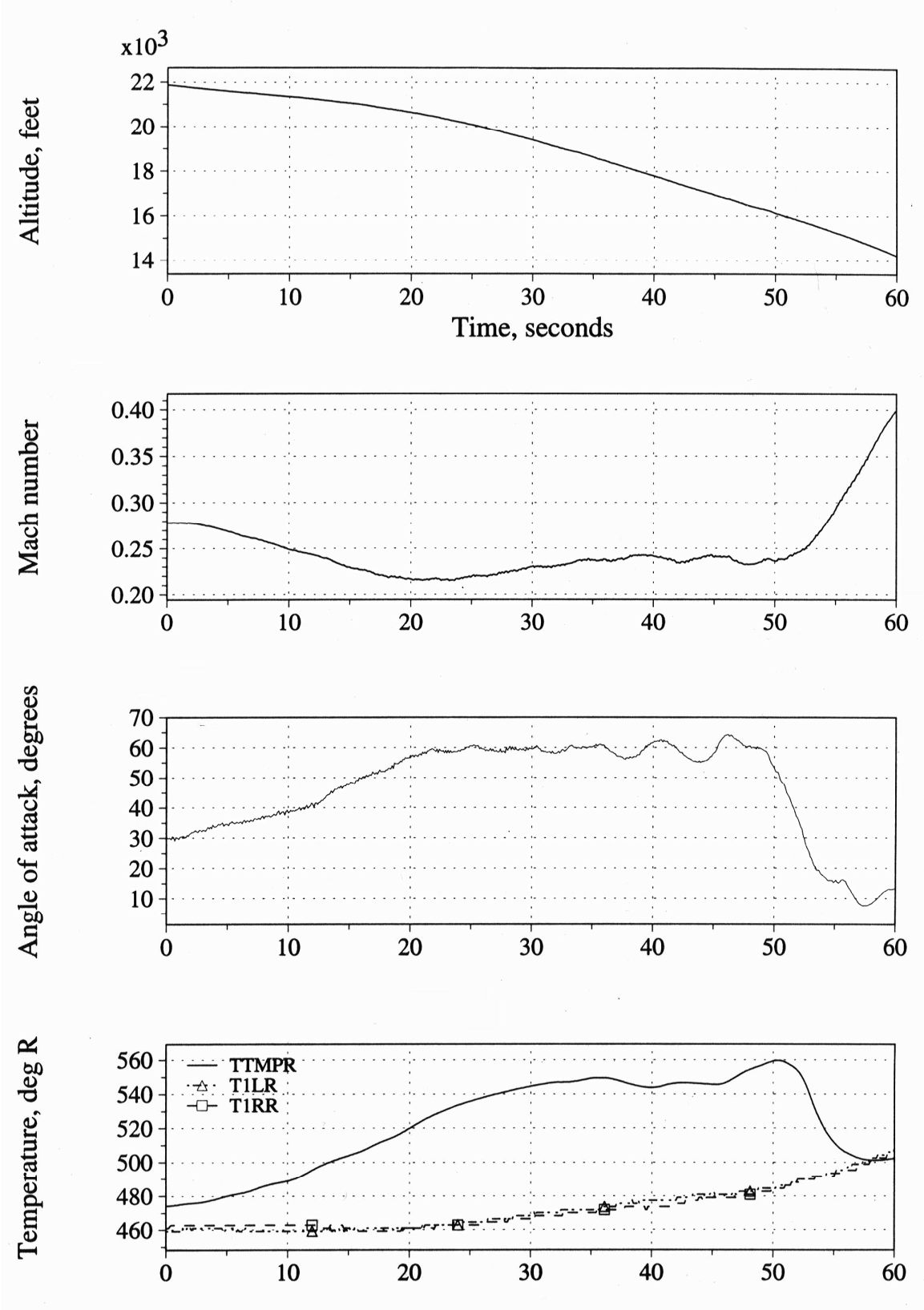

Figure B1. Illustration of temperature probe differences during angle-of-attack-change.

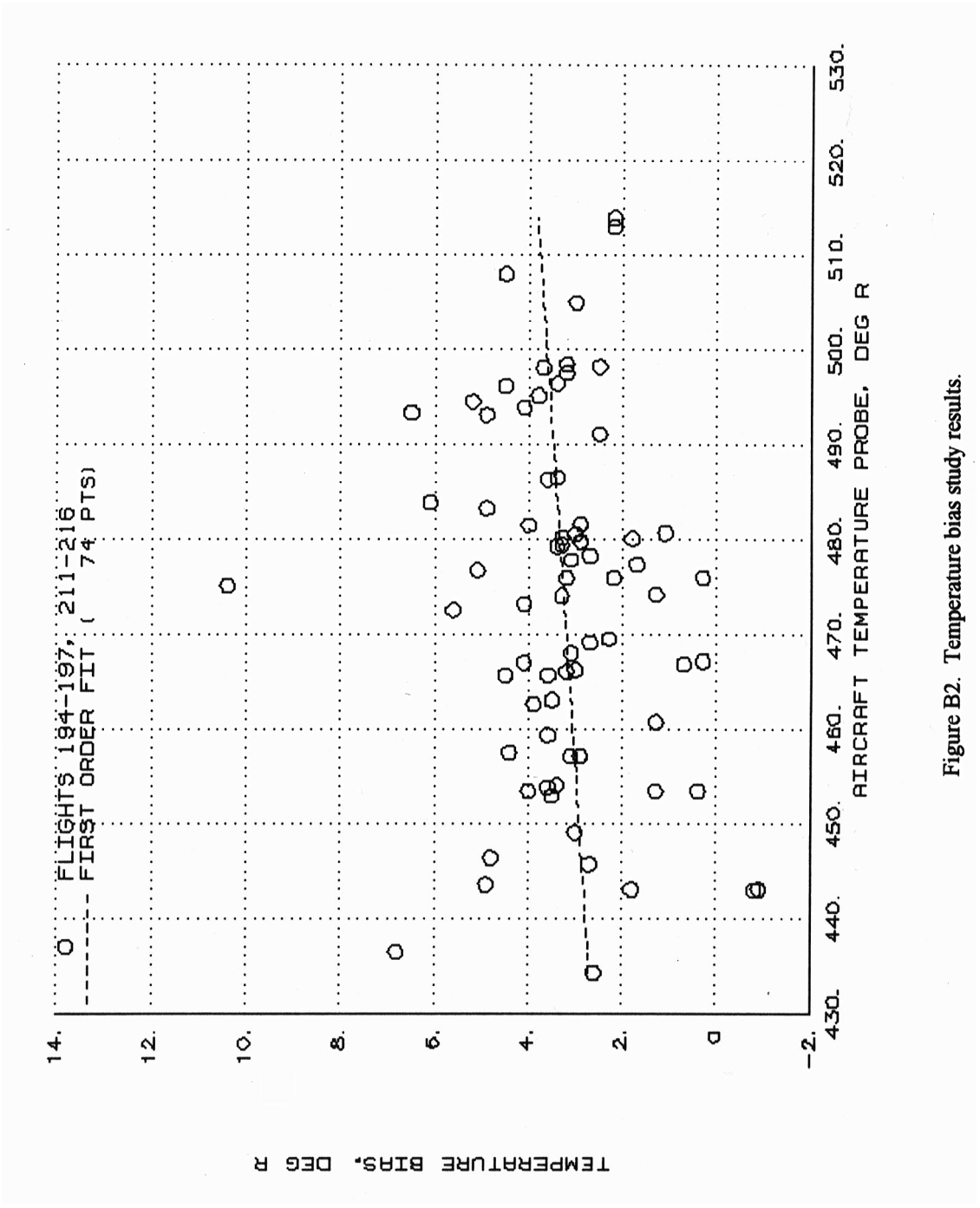

Figure B2. Temperature bias study results.

APPENDIX C - AIRFLOW CORRELATION STUDY DATA SUMMARY

The following tables provide tabular summaries of the data that were used in establishing the in-flight airflow correlations with clean inlet flow and the data that were obtained at stabilized attitude points.

Table C1 data used to establish the in-flight airflow correlations are grouped by Mach number and then are sorted in ascending order of airflow.

Table C2 inlet maneuver condition data were obtained at Mach 0.3 and are grouped by angle of attack and then are sorted in ascending order of sideslip.

Table C3 inlet maneuver condition data were obtained at Mach 0.4 and are organized in a manner similar to the Table C2 data.

Table C1. In-flight airflow correlation conditions.

Flight/tp	Flight Conditions				Power	Ao/Ac	AIP St-St Spatial Distortion			Turb.	Planar Wave	Corrected Airflow - lb/sec			
	Mach	AOA	AOSS	Altitude			ΔP/PC Max	ΔP/PR Max	Wall Static			f(Speed)	Uncorrelated Values		
		Deg.	Deg.	Ft.			Circumferential	Radial	(Max-Min)/Avg	RMS	Peak-to-Peak	Reference	f(AIP)avg	f(AIP)local	f(AIP)interp
233/6e	0.40	11.5	0.1	24913	Windmill	-	0.001	0.000	0.002	0.009	0.063	-	13.1	12.1	12.4
233/8e	0.39	10.7	-0.5	24944	Flight Idle	0.560	0.014	0.008	0.005	0.002	0.005	71.2	79.2	78.7	78.7
233/7b	0.40	11.7	-1.6	24846	85% N1C	0.847	0.020	0.020	0.010	0.003	0.005	108.9	117.9	117.4	117.4
234/3a	0.40	12.2	-1.2	25276	Mil	1.104	0.038	0.042	0.018	0.005	0.009	145.8	157.4	156.4	156.5
233/6d	0.60	5.2	-0.3	25032	Windmill	-	0.002	0.001	0.005	0.009	0.059	-	16.3	14.7	14.9
233/8d	0.61	4.6	1.1	25095	Flight Idle	0.393	0.014	0.009	0.006	0.002	0.004	68.2	76.9	76.4	76.4
233/7c	0.61	4.8	-0.2	25080	85% N1C	0.617	0.021	0.025	0.012	0.003	0.007	107.9	117.1	116.4	116.4
211/3g	0.59	5.1	-0.3	20175	Part Power	0.732	0.031	0.034	0.014	0.004	0.008	125.6	137.4	136.6	136.6
241/15ag	0.59	8.4	0.0	34927	Part Power	0.747	0.041	0.034	0.016	0.004	0.009	128.0	139.1	138.1	138.2
211/3f	0.60	4.6	0.2	20109	Part Power	0.809	0.026	0.045	0.018	0.003	0.008	141.1	153.4	152.5	152.5
211/3c	0.61	4.5	0.9	19974	Min A/B	0.824	0.023	0.048	0.018	0.003	0.007	145.0	156.6	155.9	155.7
211/3b	0.59	4.4	1.7	19918	Max A/B	0.836	0.019	0.047	0.017	0.003	0.008	145.1	156.8	155.9	155.9
211/3d	0.59	4.8	0.6	19994	Mil	0.836	0.025	0.048	0.018	0.003	0.008	145.1	156.6	155.6	155.7
211/3e	0.59	4.9	0.3	20086	Part Power	0.839	0.028	0.048	0.018	0.004	0.010	145.1	156.6	155.6	155.7
234/3b	0.60	5.4	0.3	25147	Mil	0.832	0.035	0.049	0.018	0.005	0.013	145.6	156.9	155.8	155.8
241/15ae	0.61	8.1	0.4	34927	Part Power	0.822	0.054	0.048	0.020	0.005	0.009	145.6	157.9	156.7	156.8
241/15ab	0.61	7.9	1.7	35026	Max A/B	0.825	0.057	0.048	0.021	0.004	0.007	146.0	157.2	155.9	156.0
241/15af	0.60	8.1	0.6	34936	Part Power	0.828	0.054	0.047	0.020	0.004	0.009	146.0	157.5	156.3	156.3
241/15ac	0.61	8.7	1.7	34921	Min A/B	0.823	0.057	0.047	0.021	0.004	0.008	146.0	157.5	156.3	156.3
241/15ad	0.60	8.2	0.6	34955	Mil	0.832	0.054	0.048	0.020	0.004	0.008	146.0	157.5	156.3	156.3
233/6c	0.81	2.8	0.4	25207	Windmill	0.072	0.003	0.001	0.007	0.006	0.037	14.4	25.9	25.4	25.5
233/8c	0.80	3.8	0.1	25293	Flight Idle	0.328	0.016	0.008	0.006	0.003	0.006	64.8	73.1	72.1	72.1
233/7d	0.81	2.7	-0.2	25105	85% N1C	0.556	0.032	0.026	0.010	0.003	0.006	110.6	120.7	119.7	119.7
234/3c	0.80	3.0	0.5	25107	Mil	0.726	0.039	0.050	0.021	0.004	0.009	144.9	156.9	155.8	155.8
233/6b	0.86	2.5	0.9	25240	Windmill	0.095	0.004	0.001	0.007	0.004	0.029	15.6	22.5	20.6	20.3
233/8b	0.87	2.2	1.1	25222	Flight Idle	0.314	0.015	0.008	0.006	0.003	0.005	63.5	71.1	70.1	70.2
233/7e	0.88	2.2	0.5	25141	85% N1C	0.540	0.026	0.025	0.010	0.003	0.007	109.8	119.7	118.7	118.7
234/3d	0.90	2.2	0.7	25059	Mil	0.704	0.030	0.050	0.021	0.004	0.009	144.4	156.7	155.5	155.6

Table C2. Inlet data maneuver conditions, Mach ~0.3.

Flight/tp	Flight Conditions				Power	Ao/Ac	AIP St-St Spatial Distortion			Turb.	Planar Wave	Corrected Airflow - lb/sec					Delta Airflow (%)			
	Mach	AOA	AOSS	Altitude			ΔP/PC Max	ΔP/PR Max	Wall Static			f(Speed)	Correlation Method				wrt Airflow f(Speed)			
		Deg.	Deg.	Ft.			Circumferential	Radial	(Max-Min)/Avg	RMS	Peak-to-Peak	Reference	1	2	3	4	1	2	3	4
215/08b	0.30	-8.6	-1.4	22924	Mil	1.384	0.053	0.037	0.022	0.010	0.014	145.9	144.4	144.1	144.1	145.9	-1.0	-1.2	-1.2	0.0
230/6b3	0.31	3.6	0.9	24034	Mil	1.372	0.018	0.051	0.010	0.005	0.010	146.0	145.6	145.3	145.9	145.9	-0.2	-0.4	0.0	0.0
216/14c	0.30	9.3	8.3	22016	Mil	1.404	0.021	0.049	0.011	0.005	0.010	145.8	145.7	145.4	145.4	145.8	-0.1	-0.3	-0.3	-0.1
230/12b1	0.32	9.4	0.8	21834	Mil	1.332	0.047	0.048	0.015	0.005	0.007	145.8	145.0	144.6	144.6	145.9	-0.6	-0.9	-0.9	0.0
216/14b	0.31	9.4	6.2	21086	Mil	1.359	0.022	0.047	0.011	0.004	0.009	145.7	145.7	145.5	145.5	145.9	-0.1	-0.3	-0.3	0.0
211/4b3	0.31	9.9	0.8	22638	Mil	1.381	0.045	0.048	0.016	0.005	0.009	145.7	145.0	144.7	144.7	145.9	-0.6	-0.8	-0.8	0.0
216/14d2	0.30	10.7	-5.6	22509	Mil	1.383	0.059	0.043	0.025	0.006	0.010	145.8	143.7	143.3	143.2	145.9	-1.5	-1.8	-1.8	0.0
234/06b	0.31	11.0	-7.9	22537	Mil	1.376	0.069	0.040	0.021	0.007	0.009	145.7	143.2	142.8	142.8	145.7	-1.9	-2.1	-2.1	-0.1
212/08b	0.30	20.1	0.4	22926	Mil	1.420	0.034	0.039	0.022	0.005	0.009	145.7	145.5	145.5	145.5	145.9	-0.3	-0.3	-0.3	0.0
215/10e	0.31	28.6	10.8	25294	Mil	1.370	0.045	0.044	0.022	0.007	0.012	145.9	145.0	144.7	144.7	145.9	-0.6	-0.8	-0.8	0.0
215/10d	0.31	29.0	5.0	25972	Mil	1.371	0.038	0.040	0.026	0.006	0.012	146.0	145.5	145.3	145.3	145.9	-0.3	-0.4	-0.4	0.0
234/02b	0.29	29.6	0.3	21584	Mil	1.444	0.058	0.036	0.023	0.007	0.011	145.6	145.1	145.0	145.0	145.8	-0.5	-0.6	-0.6	-0.1
211/24b	0.30	29.7	3.5	24226	Mil	1.414	0.045	0.039	0.026	0.006	0.011	145.8	145.2	145.1	145.1	145.9	-0.5	-0.5	-0.6	0.0
238/26b	0.30	29.8	-0.2	22132	Mil	1.420	0.061	0.036	0.026	0.007	0.012	145.9	145.6	145.5	145.5	145.9	-0.2	-0.3	-0.3	0.0
212/02b	0.30	29.8	0.4	23176	Mil	1.424	0.061	0.036	0.027	0.007	0.012	145.6	145.0	144.9	144.9	145.9	-0.6	-0.7	-0.7	0.0
232/02b	0.29	29.9	0.3	25052	Mil	1.434	0.060	0.037	0.026	0.007	0.014	146.0	145.4	145.3	145.3	145.9	-0.3	-0.4	-0.4	0.0
215/02b	0.30	29.9	0.6	25782	Mil	1.381	0.060	0.037	0.027	0.007	0.013	146.0	146.0	145.9	145.8	145.9	0.1	0.0	0.0	0.0
216/02b	0.31	29.9	0.9	24828	Mil	1.374	0.056	0.037	0.027	0.007	0.012	145.9	145.9	145.8	145.8	145.9	0.0	-0.1	-0.1	0.0
214/02b	0.30	29.9	1.0	26301	Mil	1.384	0.057	0.037	0.027	0.007	0.011	146.0	146.0	145.9	145.9	146.0	0.1	0.0	0.0	0.1
215/10b	0.29	30.0	-3.4	23660	Mil	1.434	0.068	0.035	0.031	0.009	0.013	145.9	145.3	145.1	145.1	145.9	-0.4	-0.5	-0.6	0.0
211/02b	0.30	30.0	0.3	25405	Mil	1.417	0.061	0.037	0.027	0.007	0.013	145.8	145.5	145.4	145.4	145.9	-0.3	-0.3	-0.4	0.0
213/02b	0.30	30.1	0.2	25916	Mil	1.420	0.062	0.037	0.027	0.007	0.012	145.8	145.6	145.5	145.4	145.9	-0.2	-0.3	-0.3	0.0
241/26b	0.30	30.1	0.3	25118	Mil	1.415	0.060	0.037	0.025	0.007	0.012	145.8	145.1	144.9	144.9	145.9	-0.5	-0.7	-0.7	0.0
211/25b	0.29	30.1	6.4	23818	Mil	1.441	0.042	0.041	0.026	0.007	0.013	145.8	145.0	144.8	144.7	145.9	-0.6	-0.8	-0.8	0.0
211/25c	0.31	30.4	-8.3	25603	Mil	1.344	0.069	0.036	0.035	0.010	0.014	145.8	144.5	144.1	144.0	145.9	-1.0	-1.2	-1.3	0.0
211/24c2	0.31	30.5	-2.8	27095	Mil	1.359	0.071	0.037	0.030	0.009	0.016	145.9	145.4	145.2	145.2	145.9	-0.3	-0.5	-0.5	0.0
215/10c	0.28	30.8	-7.8	22828	Mil	1.484	0.064	0.035	0.033	0.009	0.012	145.8	144.5	144.3	144.2	145.9	-1.0	-1.1	-1.2	0.0
230/02b	0.31	31.0	-0.3	25623	Mil	1.373	0.066	0.036	0.027	0.008	0.013	146.0	145.4	145.2	145.2	145.9	-0.3	-0.5	-0.5	0.0
230/02c	0.31	31.0	8.8	24490	Mil	1.384	0.045	0.043	0.022	0.007	0.012	145.9	144.4	143.9	143.9	145.9	-1.0	-1.4	-1.4	0.0
247/08b	0.29	37.8	4.0	21533	Mil	1.414	0.065	0.038	0.031	0.009	0.012	145.7	144.9	144.5	144.4	145.9	-0.7	-1.0	-1.0	0.0
212/09b	0.30	39.6	0.3	23645	Mil	1.384	0.076	0.036	0.035	0.010	0.014	145.7	144.4	144.0	143.9	145.9	-1.0	-1.3	-1.4	0.0
247/08d	0.29	40.3	-3.5	21658	Mil	1.428	0.077	0.034	0.035	0.010	0.015	145.7	145.3	145.0	144.8	145.8	-0.4	-0.6	-0.7	-0.1
231/03d	0.30	48.5	5.2	19730	Min A/B	1.389	0.071	0.042	0.039	0.012	0.016	145.6	144.4	143.6	143.6	145.8	-1.0	-1.6	-1.6	-0.1
232/3d2	0.29	48.9	-3.7	21426	Min A/B	1.403	0.076	0.040	0.046	0.014	0.017	145.9	145.4	144.4	144.2	145.9	-0.3	-1.0	-1.2	0.0
240/12b	0.30	48.9	2.9	24086	Min A/B	1.356	0.071	0.043	0.039	0.014	0.020	145.8	144.7	143.9	143.7	145.8	-0.8	-1.4	-1.5	-0.1
231/3c2	0.30	49.1	3.4	23448	Min A/B	1.353	0.073	0.043	0.040	0.012	0.017	145.8	144.8	144.0	143.8	145.9	-0.8	-1.3	-1.4	0.0
240/13b	0.31	49.2	3.1	24162	Min A/B	1.322	0.072	0.044	0.039	0.015	0.025	145.8	144.8	144.0	143.9	145.8	-0.8	-1.3	-1.4	-0.1
231/3b2	0.30	49.3	0.7	25109	Min A/B	1.355	0.076	0.046	0.042	0.015	0.028	145.9	145.2	144.2	144.1	145.9	-0.5	-1.2	-1.3	0.0
240/12c	0.30	49.4	-1.6	21622	Min A/B	1.361	0.080	0.043	0.044	0.016	0.025	145.8	145.3	144.2	144.0	145.6	-0.4	-1.2	-1.3	-0.2
213/10b2	0.30	49.4	-0.1	26601	Mil	1.356	0.078	0.047	0.043	0.016	0.022	145.9	145.6	144.5	144.3	145.9	-0.2	-1.0	-1.1	0.0
232/03d1	0.29	49.7	-4.4	24593	Min A/B	1.403	0.084	0.048	0.050	0.018	0.029	145.9	146.0	144.3	144.1	145.9	0.1	-1.1	-1.3	0.0
232/03b	0.30	49.7	1.5	24676	Min A/B	1.371	0.074	0.042	0.043	0.013	0.020	145.9	145.1	144.3	144.1	145.9	-0.5	-1.1	-1.2	0.0
232/03c	0.29	50.3	-2.8	27064	Min A/B	1.376	0.084	0.050	0.049	0.018	0.023	145.9	145.9	144.3	144.1	145.9	0.0	-1.1	-1.2	0.0
242/13c	0.30	50.6	-3.6	23595	Min A/B	1.366	0.087	0.049	0.052	0.019	0.026	145.8	146.8	145.0	144.7	145.6	0.6	-0.6	-0.8	-0.2
247/6b2	0.30	56.6	-2.2	24439	Max A/B	1.332	0.102	0.053	0.057	0.019	0.023	145.8	148.1	145.7	145.3	145.8	1.5	-0.1	-0.4	-0.1
232/05b	0.30	58.9	1.9	26855	Max A/B	1.330	0.082	0.053	0.042	0.021	0.023	145.9	147.0	145.3	145.1	145.9	0.8	-0.4	-0.5	0.0
242/16b	0.30	59.0	2.6	22229	Max A/B	1.337	0.085	0.052	0.041	0.019	0.025	145.7	147.2	145.7	145.5	145.5	0.9	-0.1	-0.3	-0.3
212/05b	0.30	59.0	2.7	25670	Max A/B	1.326	0.087	0.053	0.041	0.021	0.028	145.9	147.1	145.5	145.3	145.6	0.8	-0.3	-0.4	-0.2
243/16b	0.30	59.0	3.0	22501	Max A/B	1.306	0.085	0.051	0.041	0.019	0.022	145.7	147.0	145.6	145.4	145.6	0.8	-0.2	-0.4	-0.2
243/29c	0.32	59.1	-2.2	27126	Max A/B	1.230	0.108	0.060	0.059	0.023	0.027	145.9	149.2	146.3	145.9	145.8	2.3	0.3	0.0	-0.1
247/6b1	0.32	59.1	-0.3	26904	Max A/B	1.241	0.103	0.057	0.052	0.022	0.031	145.9	148.8	146.3	146.0	145.8	2.0	0.3	0.1	-0.1
242/17b1	0.30	59.1	1.9	28658	Max A/B	1.307	0.095	0.056	0.044	0.022	0.027	145.9	148.4	146.4	146.2	145.7	1.7	0.3	0.2	-0.1
231/04b	0.31	59.2	3.5	26076	Max A/B	1.304	0.088	0.053	0.039	0.021	0.023	145.9	147.1	145.4	145.2	145.8	0.8	-0.3	-0.5	-0.1
247/6b3	0.31	60.0	1.3	31865	Max A/B	1.268	0.102	0.057	0.045	0.024	0.029	146.0	148.6	146.6	146.4	145.8	1.9	0.5	0.3	-0.1

Table C3. Inlet data maneuver conditions, Mach ~0.4.

Flight/tp	Flight Conditions				Power	Ao/Ac	AIP St-St Spatial Distortion			Turb.	Planar Wave	Corrected Airflow - lb/sec					Delta Airflow (%) wrt Airflow f(Speed)			
	Mach	AOA	AOSS	Altitude			ΔP/PC Max	ΔP/PR Max	Wall Static			f(Speed)	Correlation Method							
		Deg.	Deg.	Ft.			Circumferential	Radial	(Max-Min)/Avg	RMS	Peak-to-Peak	Reference	1	2	3	4	1	2	3	4
215/09b	0.41	-10.3	0.2	24363	Mil	1.069	0.044	0.023	0.035	0.010	0.0159	145.9	144.4	144.6	144.6	145.9	-1.0	-0.9	-0.9	0.0
230/07b	0.40	3.7	0.4	22653	Mil	1.110	0.027	0.050	0.009	0.005	0.0085	145.8	145.8	145.6	145.6	145.9	-0.1	-0.2	-0.2	0.0
234/07c	0.41	9.3	6.8	22133	Mil	1.087	0.029	0.047	0.011	0.004	0.0066	145.6	145.8	145.7	145.7	145.7	-0.1	-0.1	-0.1	-0.1
234/07b	0.40	9.4	4.9	22099	Mil	1.114	0.026	0.046	0.011	0.004	0.0070	145.6	145.3	145.3	145.3	145.7	-0.4	-0.4	-0.4	-0.1
213/13b	0.39	9.9	0.6	22282	Mil	1.128	0.052	0.046	0.018	0.004	0.0078	145.6	144.8	144.5	144.5	145.9	-0.8	-1.0	-0.9	0.0
234/07d	0.40	10.4	-4.7	21559	Mil	1.098	0.057	0.045	0.023	0.005	0.0083	145.5	143.6	143.1	145.3	145.8	-1.6	-1.9	-0.4	-0.1
234/07e	0.41	11.0	-5.9	22964	Max A/B	1.085	0.064	0.040	0.023	0.006	0.0088	145.6	143.2	142.7	142.6	145.7	-1.9	-2.2	-2.3	-0.1
234/03a	0.40	12.2	-1.2	25276	Mil	1.104	0.038	0.042	0.018	0.005	0.0094	145.8	145.7	145.7	145.7	145.9	-0.1	-0.1	-0.2	0.0
213/14b	0.40	19.7	0.4	32134	Mil	1.106	0.033	0.043	0.023	0.005	0.0084	146.0	145.6	145.6	145.6	146.0	-0.2	-0.2	-0.2	0.1
216/11c	0.42	27.2	7.5	28986	Mil	1.064	0.035	0.041	0.022	0.005	0.0108	145.9	145.0	145.0	145.0	146.0	-0.6	-0.6	-0.6	0.1
231/05b	0.41	29.0	0.0	32536	Mil	1.085	0.038	0.042	0.024	0.007	0.0113	146.0	145.0	145.0	145.0	146.0	-0.6	-0.6	-0.6	0.1
216/11b	0.39	29.3	3.5	32229	Mil	1.141	0.040	0.040	0.023	0.006	0.0121	146.0	145.3	145.3	145.3	146.0	-0.4	-0.4	-0.4	0.1
231/19b	0.40	29.4	-0.1	28182	Mil	1.109	0.038	0.041	0.027	0.007	0.0113	145.9	145.1	145.1	145.1	146.0	-0.5	-0.5	-0.6	0.1
216/11d2	0.41	29.5	-3.8	28470	Mil	1.073	0.068	0.042	0.032	0.009	0.0142	146.0	144.8	144.5	144.5	146.0	-0.8	-1.0	-1.0	0.1
213/15b	0.41	29.9	0.2	35287	Mil	1.087	0.039	0.042	0.027	0.007	0.0123	146.0	145.1	145.1	145.1	146.0	-0.5	-0.5	-0.6	0.1
231/08b	0.40	31.3	-7.6	25843	Mil	1.085	0.075	0.039	0.034	0.012	0.0245	145.9	144.6	144.1	144.0	146.0	-0.9	-1.2	-1.3	0.1
241/10b	0.40	37.7	4.5	29065	Max A/B	1.105	0.060	0.043	0.029	0.010	0.0156	145.9	144.5	144.0	144.0	145.9	-1.0	-1.3	-1.3	0.0
243/25a1	0.40	38.3	4.1	30634	Max A/B	1.106	0.065	0.041	0.032	0.010	0.0177	145.9	146.1	145.6	145.6	145.9	0.1	-0.2	-0.2	0.0
234/08b	0.40	38.9	1.2	33550	Max A/B	1.097	0.070	0.041	0.032	0.011	0.0164	145.9	144.4	143.9	143.9	145.9	-1.0	-1.4	-1.4	0.0
241/10c	0.39	39.0	-4.0	28141	Max A/B	1.112	0.084	0.040	0.041	0.013	0.0179	145.9	145.3	144.7	144.5	145.9	-0.4	-0.8	-0.9	0.0
214/2ab3	0.40	39.2	-0.3	36178	Max A/B	1.090	0.069	0.041	0.035	0.012	0.0177	145.9	144.9	144.4	144.3	145.9	-0.7	-1.0	-1.1	0.0
235/08c	0.39	39.2	3.5	31165	Min A/B	1.117	0.066	0.042	0.031	0.011	0.0155	145.9	144.3	143.9	143.8	145.9	-1.1	-1.4	-1.4	0.0
232/04b	0.36	39.5	0.1	27855	Max A/B	1.202	0.067	0.038	0.036	0.011	0.0133	145.9	144.8	144.4	144.4	145.9	-0.8	-1.0	-1.1	0.0
233/04b	0.40	39.8	0.0	32800	Max A/B	1.086	0.072	0.042	0.035	0.011	0.0163	145.9	145.0	144.5	144.4	145.9	-0.6	-1.0	-1.0	0.0
243/25c1	0.40	40.1	-4.5	34068	Max A/B	1.086	0.086	0.040	0.041	0.013	0.0237	145.9	146.0	145.2	145.0	145.9	0.1	-0.5	-0.6	0.0

REFERENCES

1. Regenie, V., Gatlin, D., Kempel, R., and Matheny, N., "The F-18 High Alpha Research Vehicle: A High-Angle-of-Attack Testbed Aircraft," National Aeronautics and Space Administration Report TM 104253, September 1992.

2. Amin, N. F. and Hollweger, D. J., "F/A-18A Inlet/Engine Compatibility Flight Test Results," AIAA Paper No. AIAA-81-1393, July 1981.

3. Yuhas, A. J., Ray, R. J., Burley, R. R., Steenken, W. G., Lechtenberg, L., and Thornton, D., "Design and Development of an F/A Inlet Distortion Rake: A Cost and Time Saving Solution," American Institute of Aeronautics and Astronautics Paper No. AIAA-94-2132, June 1994.

4. Moes, T. R. and Whitmore, S. A., "A Preliminary Look at Techniques Used to Obtain Airdata from Flight at High Angles of Attack," National Aeronautics and Space Administration Report TM 101729, December 1990.

5. Schlichting, H., Boundary Layer Theory, Seventh Edition, McGraw-Hill, Inc., 1979, pp 42 and 638.

REPORT DOCUMENTATION PAGE

Form Approved
OMB No. 0704-0188

1. AGENCY USE ONLY (Leave blank)	2. REPORT DATE	3. REPORT TYPE AND DATES COVERED
	September 1996	Contractor Report

4. TITLE AND SUBTITLE

Estimating Engine Airflow in Gas-Turbine Powered Aircraft with Clean and Distorted Inlet Flows

5. FUNDING NUMBERS

WU 505-68-30

6. AUTHOR(S)

J.G. Williams, W.G. Steenken, and A.J. Yuhas

7. PERFORMING ORGANIZATION NAME(S) AND ADDRESS(ES)

GE Aircraft Engines
1 Neumann Way, MD A411
Cincinnati, OH 45215-6031

AS&M, Inc.
P. O. Box 273
Edwards, CA 93523

8. PERFORMING ORGANIZATION REPORT NUMBER

N/A

9. SPONSORING/MONITORING AGENCY NAME(S) AND ADDRESS(ES)

Dryden Flight Research Center
P. O. Box 273
Edwards, CA 93523-0273

10. SPONSORING/MONITORING AGENCY REPORT NUMBER

CR-198052
(H-2127)

11. SUPPLEMENTARY NOTES

Dryden Technical Monitor: Kevin Walsh. J.G. Williams and W.G. Steenken, GE Aircraft Engines, Cincinnati, Ohio. A.J. Yuhas, AS&M, Inc., Hampton, Virginia. Presented at the High-Angle-of-Attack Technology Conference, NASA Langley Research Center, Hampton, Virginia, Sept. 17–19, 1996.

12a. DISTRIBUTION/AVAILABILITY STATEMENT

Unclassified—Unlimited
Subject Category 07

12b. DISTRIBUTION CODE

13. ABSTRACT (Maximum 200 words)

The F404-GE-400 powered F/A-18A High Alpha Research Vehicle (HARV) was used to examine the impact of inlet-generated total-pressure distortion on estimating levels of engine airflow. Five airflow estimation methods were studied. The Reference Method was a fan corrected airflow to fan corrected speed calibration from an uninstalled engine test. In-flight airflow estimation methods utilized the average, or individual, inlet duct static- to total-pressure ratios, and the average fan-discharge static-pressure to average inlet total-pressure ratio. Correlations were established at low distortion conditions for each method relative to the Reference Method. A range of distorted inlet flow conditions were obtained from –10° to +60° angle of attack and –7° to +11° angle of sideslip. The individual inlet duct pressure ratio correlation resulted in a 2.3 percent airflow spread for all distorted flow levels with a bias error of –0.7 percent. The fan discharge pressure ratio correlation gave results with a 0.6 percent airflow spread with essentially no systematic error. Inlet-generated total-pressure distortion and turbulence had no significant impact on the F404-GE-400 engine airflow pumping. Therefore, a speed-flow relationship may provide the best airflow estimate for a specific engine under all flight conditions.

14. SUBJECT TERMS

Airflow correlation techniques, Airflow errors, Distorted inlet airflow, Engine airflow, GE 404 engine airflow

15. NUMBER OF PAGES

80

16. PRICE CODE

A05

17. SECURITY CLASSIFICATION OF REPORT	18. SECURITY CLASSIFICATION OF THIS PAGE	19. SECURITY CLASSIFICATION OF ABSTRACT	20. LIMITATION OF ABSTRACT
Unclassified	Unclassified	Unclassified	Unlimited

NSN 7540-01-280-5500

Available from the NASA Center for AeroSpace Information, 800 Elkridge Landing Road, Linthicum Heights, MD 21090; (301)621-0390

Standard Form 298 (Rev. 2-89)
Prescribed by ANSI Std. Z39-18
298-102